Razafindrakoto, H., Cotton, F., Bindi, D., Pilz, M., Graves, R. W., Bora, S. (2021): Regional Calibration of Hybrid Ground-Motion Simulations in Moderate Seismicity Areas: Application to the Upper Rhine Graben. - Bulletin of the Seismological Society of America, 111, 3, 1422-1444.

https://doi.org/10.1785/0120200287

Regional Calibration of Hybrid Ground-Motion Simulations in Moderate Seismicity Areas: Application to the Upper Rhine Graben

Hoby N. T. Razafindrakoto*[1], Fabrice Cotton[1,2], Dino Bindi[1], Marco Pilz[1], Robert W. Graves[3], and Sanjay Bora[4]

ABSTRACT

This study presents the coupling of the spectral decomposition results for anelastic attenuation, stress drop, and site effects with the Graves-Pitarka (GP) hybrid ground-motion simulation methodology, as implemented on the Southern California Earthquake Center (SCEC) broadband platform (BBP). It is targeted to applications in the Upper Rhine graben (URG), which is among the seismically active areas in western Europe, yet a moderate seismicity area. Our development consists of three main steps: (1) calibration of regional high-frequency (HF) attenuation properties; (2) modification of the hybrid approach to add compressional waves in the HF computation and examine various strategies to evaluate site amplification factors in the Fourier domain (e.g., V_{S30}-based or site-specific factors); (3) testing of the simulations using earthquake records from the URG ($3.7 < M_w < 5$). The validation process of the simulated time histories is performed first on rock sites, and, then subsequently at all stations, whatever their site conditions. The performance of the simulations for rock sites is assessed through the standard validation technique in the BBP (comparison of the waveforms, intensity measures, and estimation of the response spectra model bias). We additionally compare the Fourier amplitude spectrum of the simulations and observations, and compute their corresponding bias. The results show that the simulated ground motions match the general characteristics of the recorded motions, and that the model bias generally fluctuates around zero across the broadband frequency range. Hence, the hybrid ground-motion methodology implemented in the SCEC BBP can be successfully applied outside high-seismicity areas and outside those areas for which it had been generally calibrated. Our results also show that HF modification and calibration were necessary to improve the fits with the observation, and demonstrate the potential benefits of using site-specific amplification factors compared to V_{S30}-based amplification factors.

KEY POINTS

- Simulations require extensive calibration and validation to ensure their robustness for engineering application.
- The article demonstrates the importance of modifications in the Graves-Pitarka method for application to the Rhine Graben area (Europe).
- The findings support the incorporation of scenario-based simulations for use in engineering applications.

Supplemental Material

INTRODUCTION

Predictions of ground motion for future earthquake scenarios are fundamental for evaluating seismic hazard, and subsequently to perform prevention, preparedness, and response actions to reduce seismic risk. When databases of ground-motion recordings are too sparse to develop ground-motion models (GMMs) from recorded data accurately, strong-motion simulations become essential. In recent years, the development of advanced ground-motion simulation methodologies has attracted growing attention, given the significant increase of available computation power, as well as more advanced knowledge about earthquake source processes, wave propagation, and the effects of near-surface site conditions (e.g., Frankel, 2009; Graves and Pitarka, 2010; Mai et al., 2010; Zheqiang and Day, 2013; Olsen and Takedatsu, 2014; Withers, Olsen, Day, et al., 2019; Withers, Olsen, Zheqiang, et al., 2019). Such a simulation framework is fundamental, because it produces time histories that can serve as input excitation for the dynamic analysis of structures. It can also be used to complement ground-motion recordings at sites where seismic stations are not available (e.g., Bydlon et al., 2019). Nevertheless, the applicability of simulations requires extensive calibration and validation to ensure their robustness for a particular region.

Several studies have been dedicated to validating ground-motion simulation models, since the 1970s

1. GFZ German Research Centre for Geosciences, Potsdam, Germany, https://orcid.org/0000-0002-7717-280X (HNTR); https://orcid.org/0000-0002-9242-3996 (FC); https://orcid.org/0000-0002-8619-2220 (DB); https://orcid.org/0000-0002-8575-579X (MP); **2.** University of Potsdam, Potsdam, Germany; **3.** U.S. Geological Survey, Pasadena, California, U.S.A., https://orcid.org/0000-0001-9758-453X (RWG); **4.** IIT, Gandhinagar, Gujarat, India, https://orcid.org/0000-0002-2043-0513 (SB)

*Corresponding author: hoby@gfz-potsdam.de

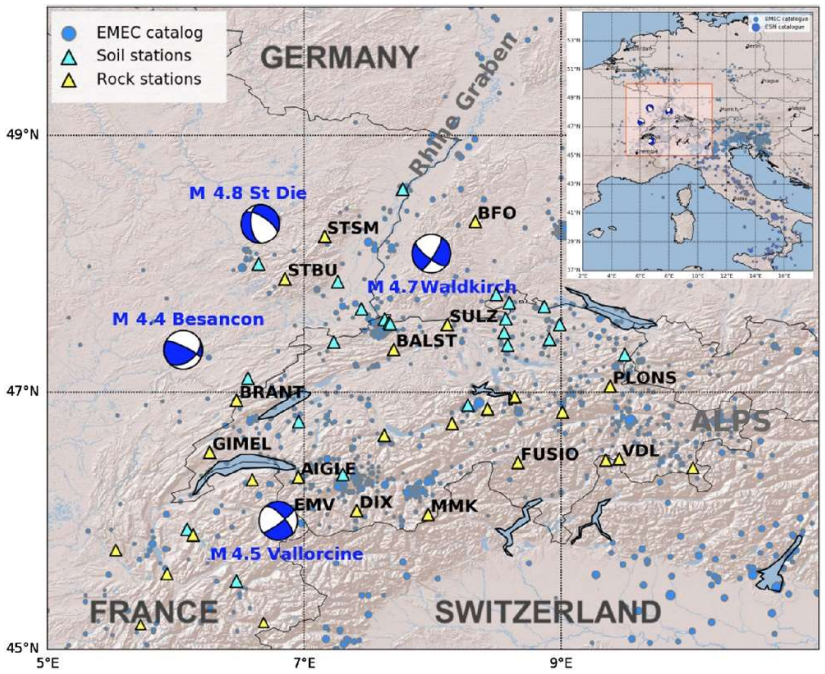

Figure 1. *Earthquake sources and ground-motion stations used in the validation (the inset map shows the location of the study area within western Europe). The blue dots in the background represent the regional seismicity in the area (Grünthal and Wahlström, 2012). EMEC, European-Mediterranean earthquake catalog.*

(e.g., Hartzell, 1978). However, given the advanced simulation methodologies and new data, further evaluations are required to enhance the reliability of predictions. The Southern California Earthquake Center (SCEC), for instance, has set up a platform to implement such a validation scheme for a collection of broadband (0–10+ Hz) simulation methods. Among these methods, there are those following a stochastic approach (e.g., EXSIM method of Atkinson and Assatourians, 2015), fully deterministic methods (e.g., composite source model, Anderson, 2015; the UCSB method developed by Crempien and Archuleta, 2015), and hybrid approaches (e.g., Graves–Pitarka [GP] method, Graves and Pitarka, 2010; the SDSU method of Olsen and Takedatsu, 2014). Most of these methods, including the GP method used in this study, pass the validation exercise evaluation criteria. By this, we mean that they were able to provide reasonable estimates of ground motion (in terms of mean log spectral acceleration [SA] values) for earthquakes within a magnitude range of 5.4–7.2 in California and in comparable active tectonic regions. Even so, it is important to note the difficulty in reproducing high-frequency (HF) motion deterministically due to the incoherence in the source radiation and wave propagation at HFs, which motivates the use of hybrid methods. Further details on the SCEC exercise and corresponding results can be found in the SRL special focus section on broadband platform (BBP) validation (e.g., Goulet et al., 2015; Dreger and Jordan, 2015). These papers also noted the necessity of further validation in terms of other applications and metrics.

The target area in this study consists of the Upper Rhine graben (URG) region, which encompasses southwest Germany, northeast France, and the northern part of Switzerland (Fig. 1). This region is located in a relatively low-earthquake hazard on a global scale (Grünthal et al., 2018). However, the potential seismic risk in this region should not be neglected, because it has experienced some damaging historical earthquakes, including the 1356 M_w 6.6 Basel earthquake, which destroyed the city of Basel and caused severe damage to buildings in the surrounding region (e.g., Fäh, Gisler, et al., 2009; the 2004 M_w 4.8 Waldkirch event, which occurred close to Freiburg and caused damage mostly in the form of cracks in walls (e.g., Schwarz et al., 2006); and the 2003 M_w 4.8 St Dié earthquake, which caused the collapse of several chimneys in the epicentral region (Dominique and Le Brun, 2003). The earthquakes in the target area mostly follow the main tectonic structures, which are the URG, the Jura Mountains, and the Alps. The URG (oriented northeast–southwest) is a part of an old rift system that was developed during the late Eocene (about 35 Ma) in a complex interaction with Alpine folding (e.g., Nivière et al., 2008). Each side of this graben is characterized by transtensional faults, which at its southern end merges into the Jura Mountains (e.g., Rotstein et al., 2006; Rotstein and Schaming, 2011).

As mentioned earlier, reproducing HF part of the shaking is challenging. So, to better constrain the HF simulation, yet using a semistochastic method, we can take advantage of all the earthquake records (even weak motions) that occurred in the area. Given the significant increase of modern recording stations density, these records have been extensively used in the past few years to evaluate critical seismic parameters, such as anelastic attenuation, stress drop, and site effects through spectral decomposition methods (e.g., Oth et al., 2011; Bindi and Kotha, 2020). Coupling the spectral decomposition results for a local region and broadband simulation methods could be beneficial not only to bind the low frequency (LF) and HF motions for the hybrid method but also to generate site-specific ground motions.

This article presents a comprehensive calibration and testing of the GP hybrid methodology

TABLE 1
List of the Events and the Corresponding Source Parameters Considered in This Study: 2003 St Dié (SED), 2004 Besançon and Waldkirch (Baer et al., 2005), 2005 Vallorcine (Fréchet et al., 2011)

Event Name	Date (yyyy/mm/dd)	Origin Time (UTC) (hh:mm:ss)	Latitude (°)	Longitude (°)	M_w	Strike	Rake	Dip	Stress Parameter (MPa)
St Dié	2003/02/22	20:41:04	48.34	6.66	4.8	174	-50	47	10
Besançon	2004/02/23	17:31:19	47.28	6.26	4.5	53	31	32	7
Waldkirch	2004/12/05	01:52:36	48.11	8.08	4.7	12	75	-15	12
Vallorcine	2005/09/08	11:27:17	46.03	6.90	4.5	316	61	-15	3

The stress parameters are based on Bindi and Kotha (2020).

implemented in the SCEC BBP using the largest earthquakes in the URG area. Such validation is a way to evaluate the potential of embedding the spectral-decomposition results into the hybrid method, which is a step toward combining the two approaches to study potential future events or generate time series at sites with no observations. The new developments include three steps: (1) calibration using spectral decomposition results of Bindi and Kotha (2020); (2) modification of the HF computation to include compressional waves and new Fourier amplification models; and (3) testing of simulations using the largest recorded earthquakes (which are still moderate magnitude earthquakes) that have occurred in URG and the surrounding areas over the past 15 yr (see Table 1).

MODIFYING THE GP METHOD FOR MODERATE SEISMICITY AREAS LIKE URG

Ground-motion simulations were performed using the method of Graves and Pitarka (2010, 2015) (GP method) implemented in the SCEC BBP (v.17.3), with additional modifications for the HF and near-surface amplification parts. In the platform, the GP method consists of a hybrid broadband ground-motion simulation approach based on frequency–wavenumber Green's functions for LF and a semi-stochastic ray theory method for HF. These separate low- and high-frequency motions are combined to produce a single time series for each component through a matching filter process. A transition frequency of 1 Hz is used, given our limited knowledge about the source and the velocity model. It should be noted that such merging frequency could be extended to higher frequencies, as sufficient detail about the source and surrounding medium, as well as complex velocity structure, are available (e.g., Graves and Pitarka, 2016). Such a method has been successfully validated for events with a magnitude range 4.7–7.2 in various regions and tectonic settings, including seismically active (western United States, e.g., Graves and Pitarka, 2010; Christchurch, e.g., Razafindrakoto et al., 2018; Lee et al., 2020) and stable continental regions (eastern North America, Graves and Pitarka, 2015). Skarlatoudis et al. (2015) also demonstrated the ability of this hybrid simulation methodology to reproduce the main characteristics of the recorded ground motions for large subduction earthquakes.

At LF, the earthquake source consists of a kinematic rupture model characterized by the spatiotemporal evolution of the rupture. The corresponding fault geometry is defined based on the scaling relationship of Leonard (2014). For instance, the 2003 M_w 4.8 St Dié earthquake consists of a fault geometry of 1.8 km×1.8 km, which looks like a point source at longer periods. The corresponding location, magnitude, and focal mechanism are obtained from centroid moment tensor solutions. The rupture model is generated using the stochastic slip generator of Graves and Pitarka (2016), in which the slip-rate function is a Kostrov-like pulse (Liu et al., 2006), and the average rupture speed is about 80% of the local shear-wave velocity. Such rupture speed is further reduced by a factor of 0.6 for depths less than 5 km, to account for the shallow crustal-weak-zone in surface-rupturing events. More details about the stochastic slip generator can be found in Graves and Pitarka (2016). Another fundamental component of the simulation is the crustal velocity structure. In this study, we have used velocity model based on Havenith et al. (2007) that has been developed for the URG area. In a similar way as the other velocity structures used in SCEC BBP, we have modified the model to incorporate shallow layers of low-seismic velocity representing weathered rock. This modification aims to have a smooth transition to the median V_{S30} (here 800 m/s), which is the travel-time averaged shear-wave velocity in the upper 30 m (Fig. S1, available in the supplemental material to this article). This average velocity model for the URG region is used to compute the Green's functions, which are subsequently uploaded to the SCEC BBP.

The HF simulation methodology used for frequencies larger than 1 Hz is a semistochastic approach that sums the response for each subfault, given the contribution of source, path, and site effects. The target subfault size is 1.0 km× 1.0 km, and these dimensions are adjusted slightly to preserve the total fault dimensions. For the 2003 M_w 4.8 St Dié earthquake, for instance, the total fault size of 1.8 km×1.8 km is divided into four subfaults with

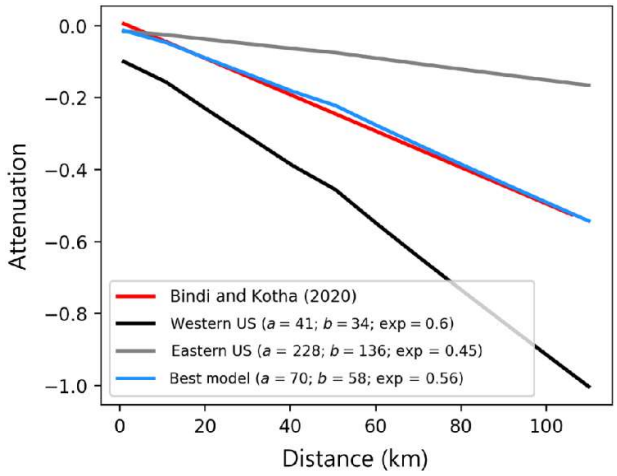

Figure 2. *Illustration of the best-fitting anelastic attenuation model at 8 Hz. Note the y axis is in log_{10} scale.*

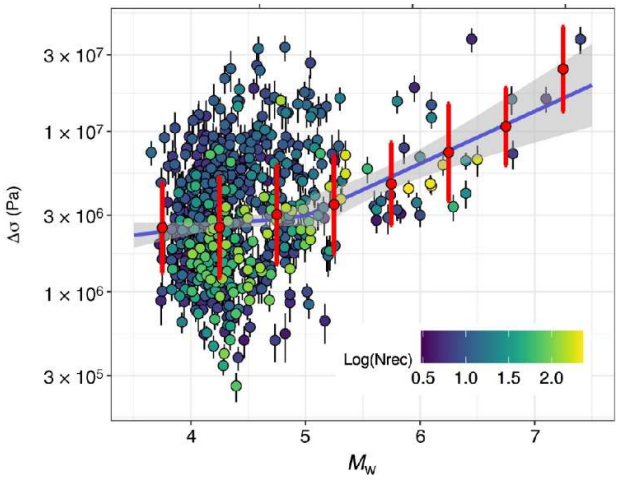

Figure 3. *Stress-drop magnitude scaling obtained by Bindi and Kotha (2020) for European earthquakes using the engineering strong-motion data. Bars presents the mean ± one standard deviation computed over bins 0.5 mu wide. The blue line is the result of a segmented regression with confidence bounds on the mean model.*

dimensions of 0.9 km×0.9 km. The slip rate function of the kinematic model is replaced with a windowed time series of bandlimited white Gaussian noise. This time series is filtered to a target omega-squared spectrum and scaled to match the target moment release on each subfault. Such a strategy is designed to utilize the random phasing of the radiated subfault waveform, to represent the poorly constrained and/or unknown details of the rupture process (Graves and Pitarka, 2010). In HF simulation, some parameters need to be tuned to be consistent with the area of study, such as the kappa value, anelastic attenuation parameters, and Brune stress parameter (stress parameter). The kappa value is a parameter introduced by Anderson and Hough (1984), to describe the spectral decay of the acceleration spectrum at high frequencies. In the simulation, it is applied as a low-pass filter to constrain high frequencies, affecting peak ground motion and spectral shape. After some parametric tests, we set a regional kappa value of 0.02 s for the URG. The anelastic attenuation and stress parameter, on the other hand, are defined based on the spectral decomposition results, which are described further in the following section.

In the standard GP method, the HF simulation generates only *S* waves. For the ground-motion simulation of large earthquakes in active regions, such missing HF *P*-wave energy is not significant, as the extended source effects dominate the waveform; however, for small events, the motion is dominated by HF motion with distinct *P*- and *S*-wave packets. In addition, in a low-seismicity region, the validation is limited due to the scarcity of data; hence, more distant recordings will also be incorporated. In this case, the missing HF *P*-wave is striking, when comparing the simulation and recorded waveforms (see Fig. S2). Therefore, we modify the standard GP method by incorporating *P*-wave energy into the HF computation. Such a modification is expected to generate only minor changes in the overall goodness of fit, in terms of response spectra (bias computation). However, it is expected to improve certain ground-motion intensity measures, such as the Arias intensity (Arias, 1970), which is commonly used in geotechnical engineering and implicitly contains information about duration, amplitude, and frequency content (e.g., Kramer and Mitchell, 2006). It would also be an important contribution for the earthquake early warning community, as the existence of *P*-wave in the synthetic waveform is of critical importance for the simulations used in early warning systems (e.g., Chen et al., 2012; Saunders and Aagaard, 2019).

In terms of near-surface site amplification, the standard GP method in the BBP utilizes V_{S30}-based site amplification factors that have been strictly developed for SA. However, these are applied to the Fourier amplitude spectrum (FAS) of the simulated time series. Therefore, we also investigate the benefits of using Fourier-based amplification. This involves empirical V_{S30}-based (Bora et al., 2019) and site-specific amplification functions derived from the decomposition of the spectral amplitudes of the engineering strong-motion (ESM) flat file data into source, propagation, and site effects (Bindi and Kotha, 2020).

CALIBRATION AND MODIFICATION OF THE SIMULATION METHOD

Coupling spectral decomposition results and the semistochastic HF simulation In this study, we have chosen to calibrate the HF motion using spectral decomposition results. Indeed, the HF part in the hybrid method of Graves and Pitarka (2010), which

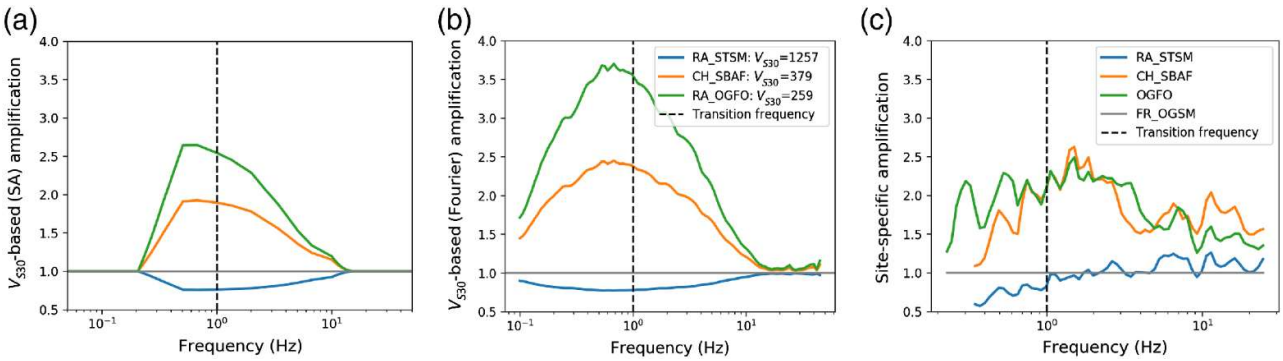

Figure 4. *Site amplification factors at three sites with various V_{S30} values. (a) Standard method (spectral acceleration [SA-based] V_{S30}), (b) Fourier-based V_{S30}, and (c) site specific.*

consists of a semistochastic procedure based on Boore (1983), requires well-calibrated source, path, and site effects within the region of interest. In the semistochastic approach, the path term is expressed as follows:

$$P(R,f) = Z(R)\exp\left[-\pi f^{1-x}\sum_{k=1}^{L}\frac{T_k}{Q_k}\right], \qquad (1)$$

in which $Z(R)$ represents the geometrical spreading of the waves, which is assumed to be a priori known (R^{-1} geometrical spreading factor), T_k is the travel time, x is the exponent of the frequency dependence of Q, and Q_k represents the HF attenuation factor in each layer k of the velocity model. The constant Q_k is modeled as a linear function of the shear-wave velocity, $Q_k = a + bV_{sk}$, with constants a and b inferred empirically. These values were set to 41 and 34 for western US earthquakes (WUS, Graves and Pitarka, 2010), and 228 and 136 for eastern North America (ENA, Graves and Pitarka, 2015), given the evidence of large Q values in the ENA region. Therefore, these parameters need to be appropriately calibrated and tuned according to the local attenuation. For the URG region, we estimate these values by fitting the anelastic attenuation term for Europe, derived from the spectral decomposition of Bindi and Kotha (2020). The adopted anelastic attenuation is based on the one generated for the region named "RE" in Bindi and Kotha (2020), which corresponds to Germany, France, the Balkans, and Romania. Figure 2 illustrates the best-fitting models at 8 Hz through the maximum likelihood approach, and the preferred values are $a = 70$, $b = 58$, and $x = 0.56$. The stress parameter also plays a fundamental role in the source description of the HF simulation and controls the spectral amplitudes. For the validation, we adopt the stress drop (i.e., stress parameter) values computed from spectral decomposition of Bindi and Kotha (2020). Figure 3 shows their stress drop versus magnitude scaling developed using the ESM data for Europe (Bindi et al., 2019). In this study, we predict ground motions using event-specific stress drops (stress parameters) to test and validate the fact that the stress drops obtained by the spectral decomposition method are consistent and can be used as input parameters of the hybrid simulation broadband method. Table 1 shows the stress parameter values corresponding to the four events analyzed in this study.

Incorporation of compressional waves in HF motion

The last HF modification consists of adding P waves to the synthetic waveform. Aside from the envelope function for S-waves in the standard GP method, which is based on Saragoni and Hart (1974), a new envelope corresponding to the P waves is considered following Pousse et al. (2006):

$$P = \frac{C}{t\sqrt{2\pi\sigma}}\exp\left[-\frac{1}{2\sigma^2}\left(\log(t)-\mu_p\right)^2\right], \qquad (2)$$

$$\sigma = \frac{1}{3}\log\frac{t_S - t_P}{T_S}, \qquad (3)$$

$$\mu_p = \log(T_P) + \sigma^2, \qquad (4)$$

The expected mean value μ_p controls the occurrence time of the maximum amplitude, and the term σ represents the standard deviation of the envelope function, which controls the duration of the P-wave packet. t represents the time, and C is the Arias intensity defined based on the European empirical GMM of Sandikkaya and Akkar (2017). The additional scaling is chosen by assuming that the S-wave amplitude is about five times larger than the P-wave amplitude in the far field. It is worth noting that the method of Pousse et al. (2006) is empirical. In equations (3) and (4), $T_P = [(t_S - t_P) + 0.25SMD/3]$, $T_S = [(t_S - t_P) + 0.25SMD]$, in which $t_S - t_P$ is the time delay between S and P waves and SMD is the strong-motion duration. The simulation approach described earlier is referred to as the modified-

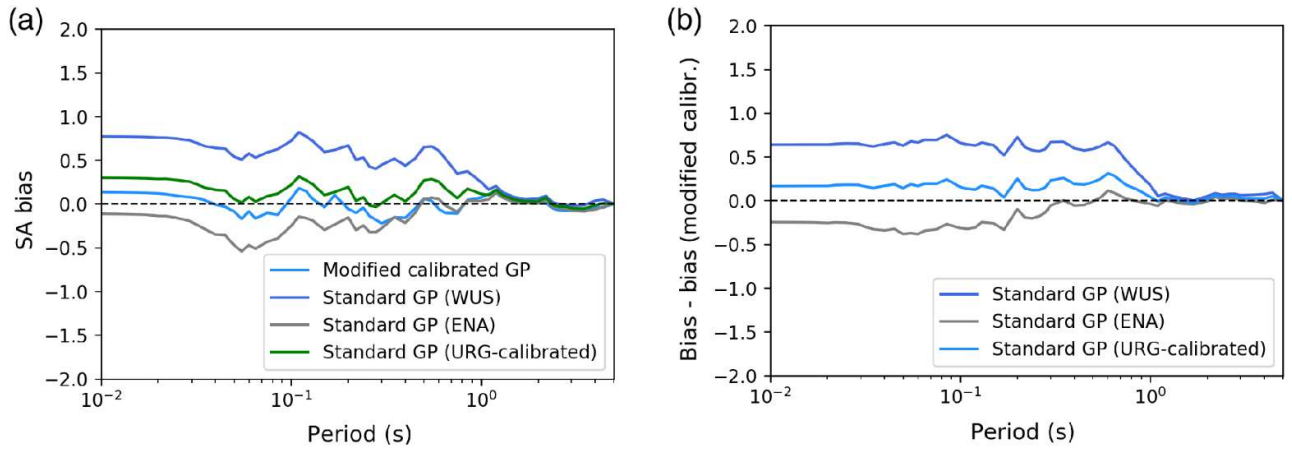

Figure 5. *(a) SA bias for the simulations of the St Dié earthquake from modified-calibrated Graves-Pitarka (GP) and standard GP methods with Eastern North America (ENA), Western United States (WUS), and Upper Rhine graben (URG) parameterizations computed using 20 rock sites. (b) SA bias differences with respect to the modified-calibrated GP method.*

calibrated GP method, hereafter. We acknowledge that rigorous *P*-wave validation is still required before applying to earthquake early warning. However, the development of empirical GMM and new metrics specific for *P*-wave validation is beyond the scope of this study and will be left for a future extension of this work.

New procedure for near-surface site amplification computation

Near-surface site amplification is among the crucial components in GMMs (both empirical and physics-based). There are several techniques to estimate this component, including: (1) empirical methods based on V_{S30}; (2) a site-specific approach using amplification factors extracted from individual recordings; and (3) numerical simulations based on an 1D *S*-wave profile. In this study, we utilize the first two techniques, as the third requires a detailed underground model of the site, which is not fully available for the target area.

This study adopts three different site amplification models. First, we use the amplification factors in the standard GP method, which come from the V_{S30}-based empirical amplification model of Campbell and Bozorgnia (2014). These factors were originally developed to be applied to response spectra; however, in the GP method, they are applied to Fourier spectra in the frequency domain. A truncation of the factors is applied at higher frequencies, to partially resolve this inconsistency (Graves and Pitarka, 2010). To apply these amplification factors to the URG, the reference surface site condition is set to 800 m/s. The location-specific V_{S30} values are retrieved from the ESM and Réseau Accelerométrique Permanent (RAP) data. The second approach consists of the V_{S30}-based model of Bora et al. (2019), which is an empirically derived Fourier model. Both V_{S30}-based empirical amplification models have been calibrated on Next Generation Attenuation-West2 Project data. The third approach is the site-specific amplification model of Bindi and Kotha (2020), derived from spectral decomposition analysis. Bindi and Kotha (2020) performed their study for Europe and the Middle East, by analyzing the FAS of all earthquakes with magnitudes greater than 4 occurring in these regions, and recorded by at least three stations. Three of the events used in our study were among the selected ones from that work. The St Dié event was not among those selected, because it has only a few records. The derived site-amplification models are available for stations in the ESM flat

TABLE 2
List of Methods and Parameterizations Used in This Study

		Attenuation Parameters			
Method	HF *P* Waves	*a*	*b*	exp	Site Amplification (All Sites)
Standard GP (ENA parameterization)	No	228	136	0.45	V_{S30}-based (SA)
Standard GP (WUS parameterization)	No	41	34	0.6	V_{S30}-based (SA)
Standard GP (URG parameterization)	No	70	58	0.56	V_{S30}-based (SA)
Modified-calibrated GP	Yes	70	58	0.56	V_{S30}-based (SA) V_{S30}-based (Fourier) Site specific

ENA, Eastern North America; GP, Graves-Pitarka; URG, Upper Rhine graben; WUS, western United States.

file with at least four recordings that pass quality check criteria. Hence, they are not available for all sites used in the validation. The derived amplification factors are relative to stations that have almost flat amplifications relative to a reference site condition, which are mostly located on rock sites with average V_{S30} values of about 800 m/s. Figure 4 illustrates the frequency-dependent site amplification factors from these three approaches at three stations with different site conditions (V_{S30} values of 259, 379, and 1257 m/s).

Validation steps

For the validation, we use four earthquakes that are among the most significant events that occurred in the URG region over the past 15 yr (listed in Table 1). Figure 1 shows the location of these earthquakes and the strong-motion stations (within 300 km from the sources). The data have been retrieved from three databases: the European Integrated Data Archive (EIDA), the ESM data for Europe (Bindi et al., 2019), and the French accelerometric network (RAP) datasets (Traversa et al., 2020).

To highlight the salient effects of the calibration and the modification in the GP method, we present the results in three stages. First, we examine the relative performance of the GP method considering different anelastic attenuation parameterizations (ENA, WUS, and URG) and the modified-calibrated GP for one event. Subsequently, simulation results from three additional events are presented by applying the modified-calibrated GP and considering only stations on rock sites. These stations are obtained from Pilz, Cotton, Kotha (2020) and were selected based on surface geology, the slope of the topography, horizontal-to-vertical spectral ratios, and local magnitude station correction. To analyze the validity of the simulation results and their corresponding input parameters, comparisons between data and simulations are carried out in terms of ground-motion waveforms along with their corresponding intensity measures, including peak ground acceleration (PGA), peak ground velocity, and SA at various vibration periods. The performance assessments are conducted, considering individual sites as well as ensemble statistics for a set of strong-motion recording sites. Here, we also analyze the FAS and its corresponding bias. This bias is similarly defined as the response-spectra model bias (Graves and Pitarka, 2010), which is the residual distribution over all stations j, with a mean value of:

$$M(T_i) = \frac{1}{N}\sum_{j=1}^{N}\{\ln[IM^j_{Obs}(T_i)] - \ln[IM^j_{Sim}(T_i)]\}, \quad (5)$$

in which $IM^j_{Obs}(T_i)$ and $IM^j_{Sim}(T_i)$ are the observed and simulated intensity measures (FAS or SA), respectively, on a given component and at period T_i, and N is the number of stations. Finally, we investigated the performance of the three site-amplification models, as illustrated in Figure 4, at all stations.

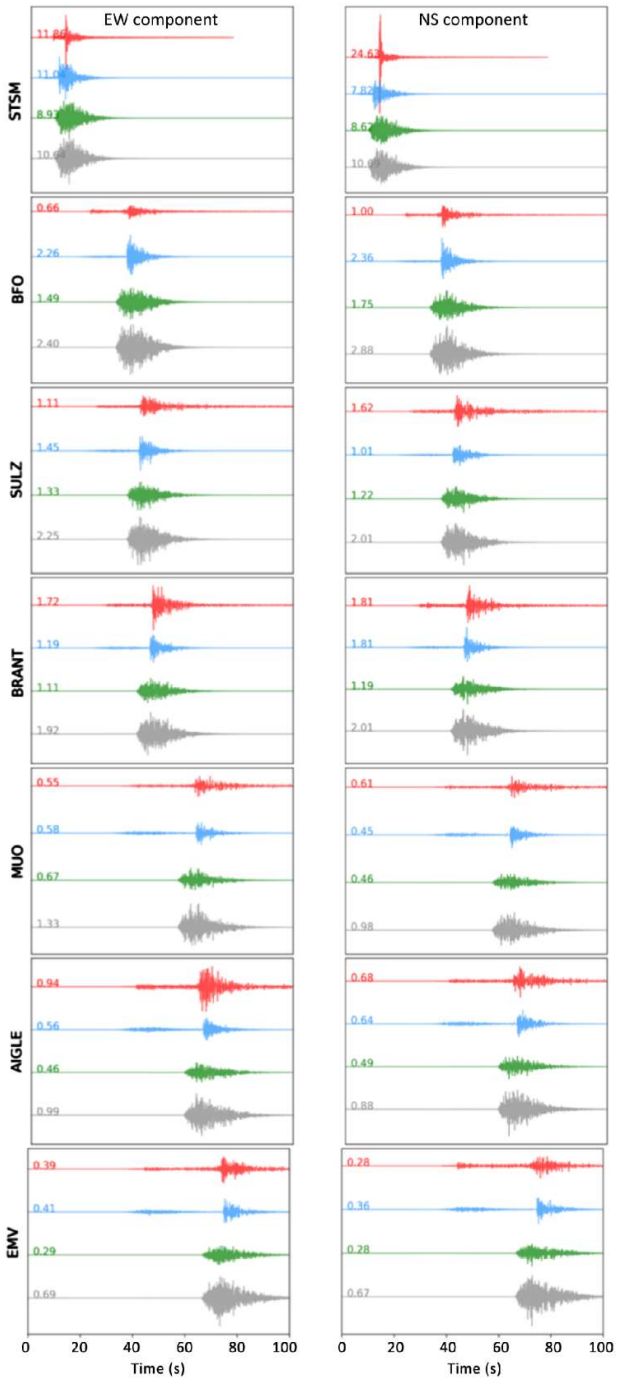

Figure 6. *Comparison of the acceleration waveforms at seven representative stations on rock sites: (top) observed; (second) modified-calibrated GP; (third) standard GP (URG calibrated); (bottom) standard GP (ENA parameterization). The maximum acceleration (cm/s²) for each waveform is shown above each trace.*

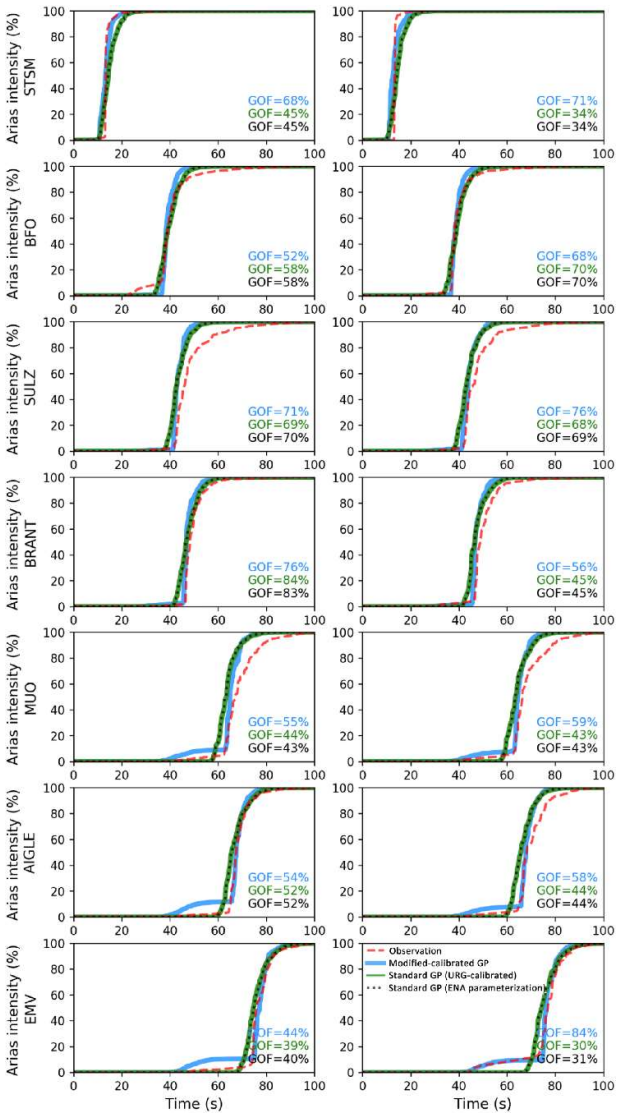

Figure 7. *Comparison of Arias intensities at seven representative stations on rock sites: observed (dashed line), modified-calibrated GP (solid thick line), standard GP (URG calibrated) (solid thin line), standard GP (ENA parameterization) (dotted line). The goodness of fit of each Arias intensity is shown on the left of each graph.*

COMPARISON OF THE STANDARD AND MODIFIED GP METHOD AT ROCK SITE: 2003 M_w 4.8 ST DIÉ EVENT

As an illustrative example, simulation results from the 2003 M_w 4.8 St Dié event are presented to provide insight into the adequacy of the URG calibration and the modification in the HF computation. This event struck eastern France, at 48.34°N, 6.66°E, with a depth of about 10 km on 22 February 2003 at 20:41 UTC, as reported by the French seismic monitoring agency (Réseau National de surveillance sismique [ReNaSS]). The focal mechanism reported by the Swiss Seismological Service (SED) has strike, dip, and rake of about 174°, 47°, and −50°, respectively (Table 1), which is consistent with normal faulting accompanied by some strike-slip component. For this event, a stress parameter of 10 MPa was used for the HF computation. This value is set following Scherbaum et al. (2004), who suggested a relatively high-stress parameter (>8 MPa) for the St Dié earthquake when compared with the average stress parameter in the active parts of Europe. Similarly, Bora et al. (2017) suggested a relatively large stress-drop value for this earthquake.

We performed the ground-motion simulations for this event using the standard GP (ENA, WUS, and URG-calibrated) and the modified-calibrated GP methods. The differences between these methods are listed in Table 2. Figure 5 compares the goodness of fit in terms of SA bias, considering these four cases at rock sites. The standard GP method, incorporating the calibration of anelastic attenuation for central Europe (URG calibrated), provides a much better fit to the average level of ground motion relative to that obtained with the WUS and ENA attenuation parameters. The use of the WUS parameters, for instance, tends to underestimate the observations throughout the entire HF period range. By contrast, the ENA parameters overpredict the observations, particularly, over the period range 0.04–0.2 s. The additional incorporation of the P waves (modified-calibrated GP) further decreases the bias. This leads to relatively small residuals with the most significant mean residual of about −0.3 natural log units, occurring at roughly $T = 0{:}08$ s, and having practically no bias beyond that period. We further compare in Figure 5 the SA bias with respect to the modified-calibrated GP, which quantifies the influence of the changes to the wave envelope and anelastic attenuation parameters with respect to the spectral intensity measures. The calibration of the attenuation parameter plays a scaling role over the HF part (i.e., shorter vibration periods, $T < 1$ s). It affects the SA bias uniformly and gets smaller toward $T = 1$ s (transition between LF and HF approaches). The modification of the envelope function, on the other hand, produces a uniform effect only at vibration periods of $T < 0.1$ s.

To examine further the performance of these methods, we compare the waveforms, Arias intensities, and SA (see Figs. 6–8) at seven representative stations. Given that the WUS parameterization yields the worst fits in Figure 5, we do not consider it in the following assessment. Figure 6 presents the acceleration waveforms, considering the standard GP (ENA), standard GP (URG calibrated), and the modified-calibrated GP methods along with the observations. The new envelope (modified-calibrated GP) appears to improve the characteristics of the overall waveform. There is also an improvement in the fits of the time evolution of the ground motion. Figure 7 shows the normalized Arias intensity (AI), which is the cumulative ground-motion measure computed based on the squared acceleration time integral. The

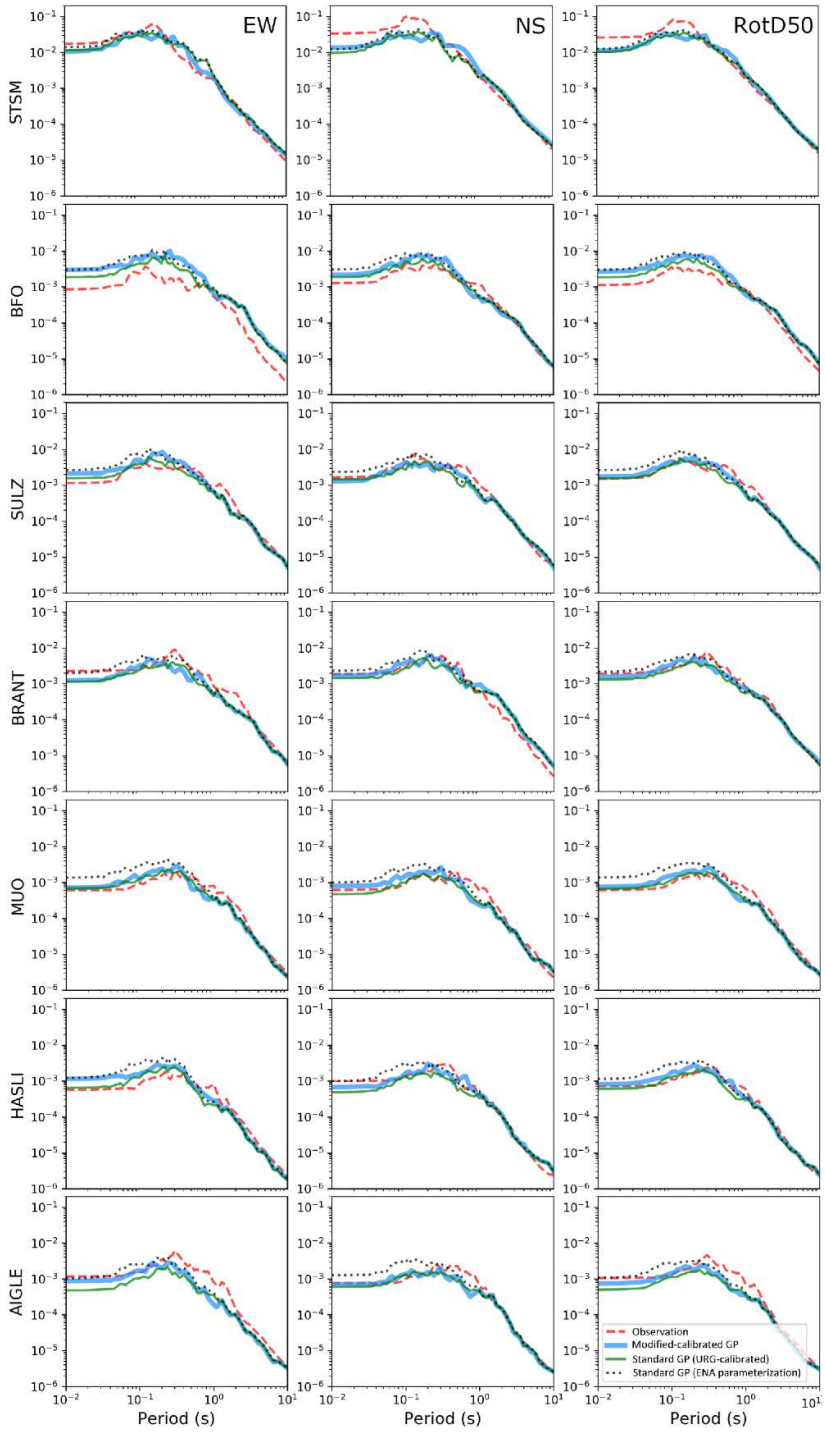

Figure 8. *Comparison of the SA (g) at seven representative stations on rock sites: observed (dashed line), modified calibrated GP (solid thick line), standard GP (URG calibrated) (solid thin line), standard GP (ENA parameterization) (dotted line).*

curves correspond to the three simulations and the observations. The three numbers in each plot are the corresponding goodness-of-fit (GOF) values calculated using the formulation of Olsen and Mayhew (2010), for which a higher GOF value represents a better fit to the observations. We found a highly variable fit. For some stations (e.g., AIGLE), the Arias intensity from the modified-calibrated GP method shows some differences compared to those of the two standard GP approaches, particularly, at the lower bound of the cumulative value due to the additional P waves in the HF motion. For others (e.g., MUO), we also notice systematic differences in the upper bound between the observations and the three simulations. These stations are mostly located in the Préalpes area, and the differences occur due to the missing coda waves in the HF, which is beyond this article's focus. In terms of the averaged AI GOF over all stations, the modified-calibrated GP method is closer to the observation, with east–west and north–south component GOFs of 63% and 60%, respectively. The two standard GP approaches have lower GOFs of 46% and 47% for the east–west component, and 50% for the north–south components, respectively.

Regarding the SA, Figure 8 illustrates the simulated response spectra resulting from these three methods and parameterizations, as well as their comparison with the observations. In general, the standard GP (URG calibrated) and the modified-calibrated GP methods provide better predictions of the observed ground motion than the standard GP (ENA). We also observed that the standard GP (ENA) systematically overestimated the SA at short periods, for stations located at larger distances from the source. These comparisons of the waveforms, Arias intensities, and SA clearly illustrate that various intensity measures are sensitive to different ground-motion aspects. For instance, the Arias intensity is more sensitive to the arrival times of the wave packets, and leads to the relative similarity of the standard GP (ENA) and standard GP (URG calibrated) methods. By contrast, the SA is more dependent on the response of the amplitude at a particular period. Hence, the predictions from the standard GP (URG calibrated) and the modified-calibrated GP methods are more similar. These results indicate that the modified-calibrated GP method yields an overall closer agreement to observations than the standard GP method. Further examination of the modified-calibrated GP method's performance is discussed in subsequent sections.

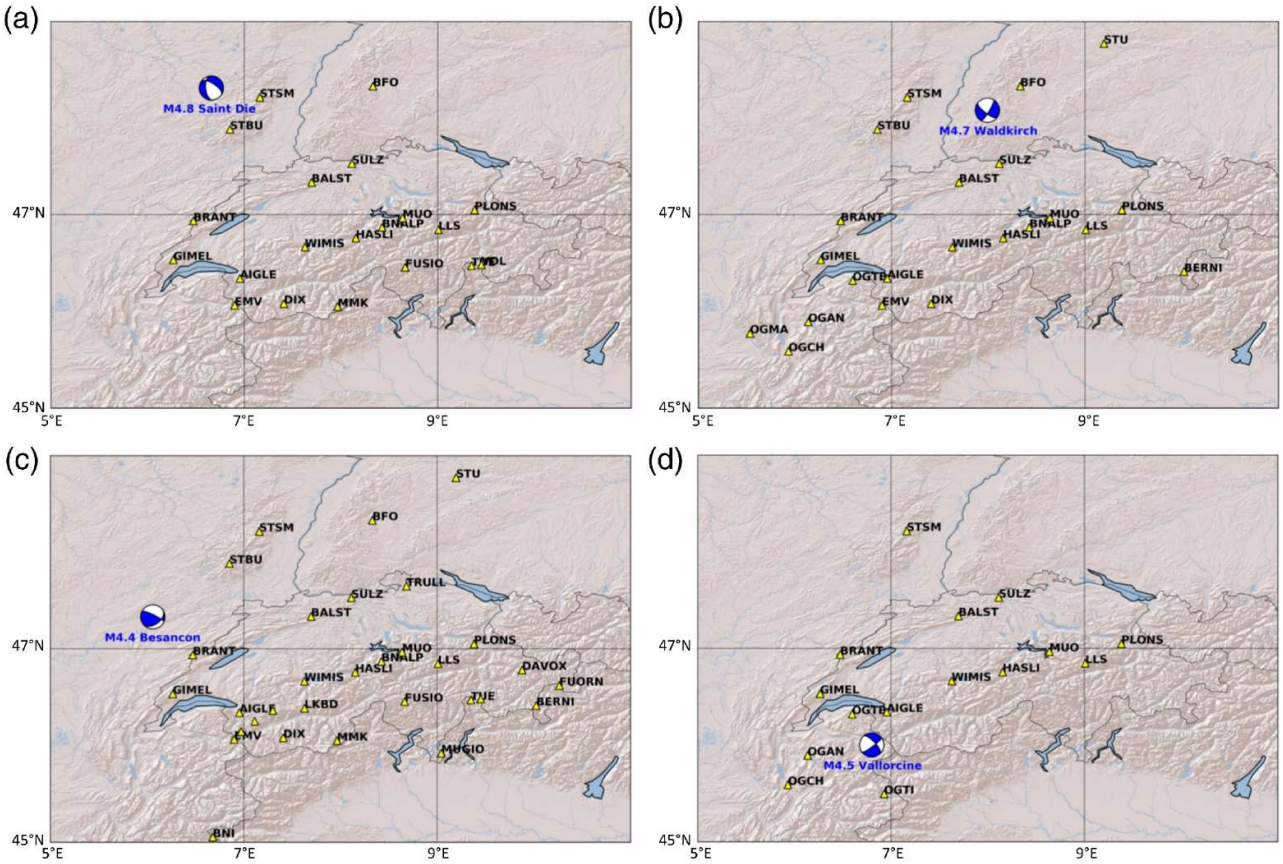

Figure 9. *Source-station geometry for each event: (a) St Dié, (b) Waldkirch, (c) Besançon, and (d) Vallorcine (see Table 1).*

TESTING OF THE MODIFIED-CALIBRATED GP METHOD (ROCK SITES)

This section further investigates the performance of the modified-calibrated GP method on rock sites. In addition to the 2003 M_w 4.8 St Dié earthquake, we applied the modified-calibrated GP method, to simulate the ground motion for three other earthquakes that occurred in the URG: the 2004 M_w 4.7 Waldkirch, the 2004 M_w 4.5 Besançon, and the 2005 M_w 4.5 Vallorcine earthquakes (Figs. 1 and 9). The size of the faults for these events was estimated using the scaling relationship of Leonard (2014). The M_w 4.7 Waldkirch event occurred on 5 December 2004 at 01:52 UTC in the Baden–Württemberg area (southwestern part of Germany). The hypocenter of this event is located at 48.11°N, 8.08°E at a depth of 12 km. It was reported to be the strongest earthquake in southwestern Germany, since the 1978 M_L 5.7 Swabian Jura earthquake. It was felt within a radius of 200 km, with a maximum intensity of VI, European Macroseismic Scale 1998 (EMS-98) (Grünthal et al., 1998; Schwarz et al., 2006). The mechanism of this event consisted of strike-slip motion. The second event is an earthquake that occurred about 23 km from Besançon (France) on 23 February 2004 at 17:31 UTC. The hypocenter of this event was located at 47.28°N, 6.26°E at a depth of about 10 km, as reported by ReNaSS. It consisted of thrust faulting, related to the crustal structure of the Jura thrust (Molliex et al., 2011). The reported magnitudes for this earthquake show a wide range with M_w 4.5–5.1. In the simulation, we adopted M_w 4.5, as reported in the ESM data, and a stress parameter of 7 MPa, which is within the stress parameter range reported by Hintersberger et al. (2007) (5–8 MPa). The third event consists of the M_w 4.5 Vallorcine earthquake, which occurred in the French Alps, near the Swiss border (at 46.03°N, 6.9°E at a depth of about 5 km) on 08 September 2005 at 11:27 UTC. According to Cara et al. (2007), the maximum intensity produced by this earthquake reached values of V, EMS-98, with slight damage in the Vallorcine and Martigny areas (about 13 km from the epicenter). It triggered some rock falls in the Mont Blanc and Aiguilles Rouges massifs. The source mechanism for this event consisted of a predominantly strike-slip mechanism, with a strike of 56°–60°, dip of 65°–84°, and rake of 169°–180° (Deichmann et al., 2006; Fréchet et al., 2011).

The obtained ground-motion results consist of a three-component time series at each seismic station (see Fig. 9). The corresponding ground-motion intensity measures, including FAS and response

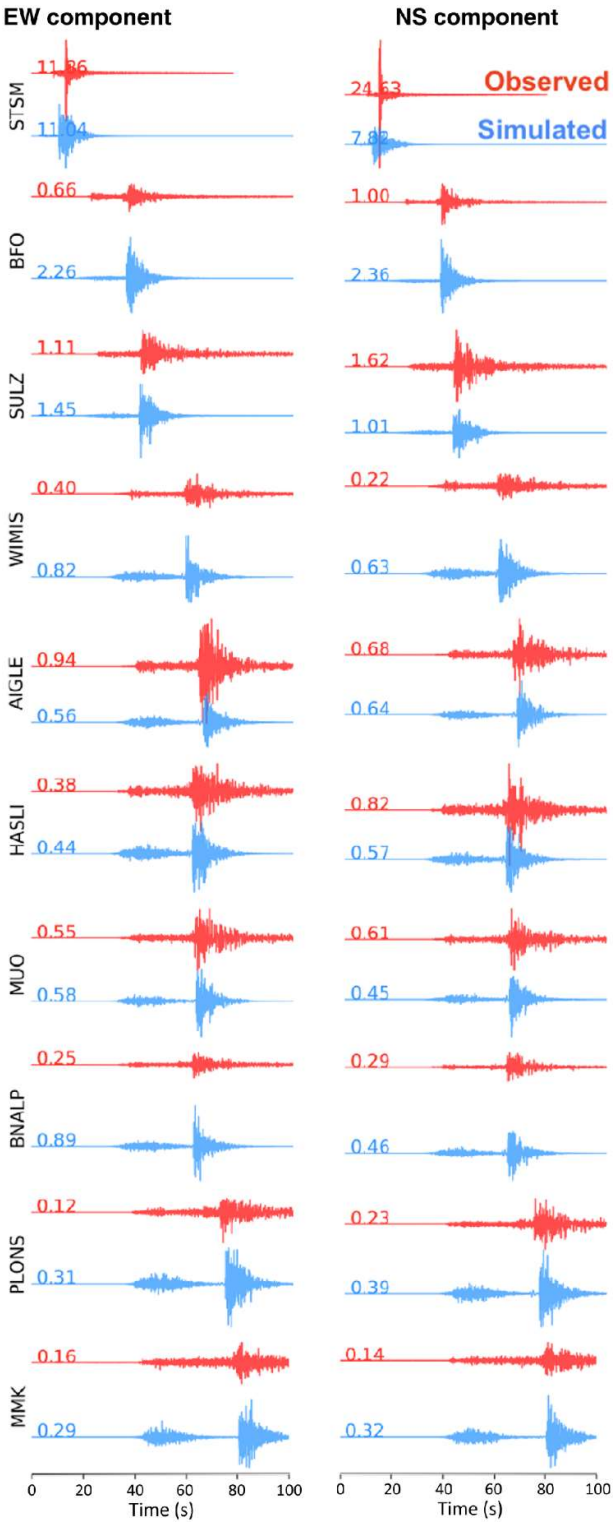

Figure 10. *East–west (EW) and north–south (NS) components of the acceleration–time series at 10 seismic stations located on rock site for the 2003 M_w 4.8 St Dié event. The maximum acceleration (cm/s²) for each waveform is shown above each trace.*

spectra (5% damped), are subsequently computed. To develop a conceptual understanding of the performance of the ground-motion simulation, we compare the synthetic ground motion with both the observations and the empirical GMM of Bindi et al. (2017).

2003 M_w 4.8 St Dié event

Because we have already presented the simulation results for the 2003 M_w 4.8 St Dié event, the following closely examines the performance of the simulations derived from the modified-calibrated GP method with respect to the observed ground motion. Figure 10 compares the observed and simulated acceleration time series at 10 representative rock sites. It illustrates that the arrival times are relatively consistent between simulated and observed ground motions, although, there is more variability in amplitudes. In general, the duration of the simulated ground motion appears to match the observed ground motion relatively well for most of the records, despite the missing coda part in our HF method. However, the recordings from a couple of stations, such as WIMIS, MUO, and HASLI (see Fig. 10), tend to have a slightly longer duration compared to the simulations. This was also observed in terms of the Arias intensity (see Fig. 7). These stations are mostly located in the Préalpes area (Lombardi et al., 2008), and such a longer duration is potentially due to complex lateral velocity structure and attenuation characteristics around this area (e.g., Edwards et al., 2011). In addition, the horizontal-to-vertical (H/V) study of Fäh, Fritsche, et al. (2009) at sites MUO and HASLI showed a small peak at about 1.6 Hz, which they interpreted to be related to some topographic effect and some changes in the velocity of the bedrock at greater depth. Figure 11 shows FAS comparisons between the simulations and observations. In general, they exhibit similar trends and features. However, some discrepancies appear at higher frequencies (>10 Hz) and around 1 Hz for some stations. To obtain a quantitative comparison of the goodness of fit between the observed and simulated ground motion, Figure 12 presents a summary of the SA and FAS bias and their corresponding variability. The black lines show the mean (natural log) residual over the 20 simulated stations; the blue bands represent plus and minus one standard deviation from the mean, and the gray band represents the 90% confidence interval of the mean. The SA bias shows, on average, a near-zero mean bias, indicating that the simulated SA values are consistent with the ground-motion recordings. The standard deviation is around 0.3 for long periods, which then increases to about 0.6 at shorter periods. In terms of the FAS bias, the simulations overpredict the observed ground motion outside the frequency range of 0.5–5 Hz. Such negative bias could be related to site amplification effects. Although, the simulations were performed for rock sites, many of the stations are located on very hard rock, with V_{S30} up to 2000 m/s, which may not be accurately

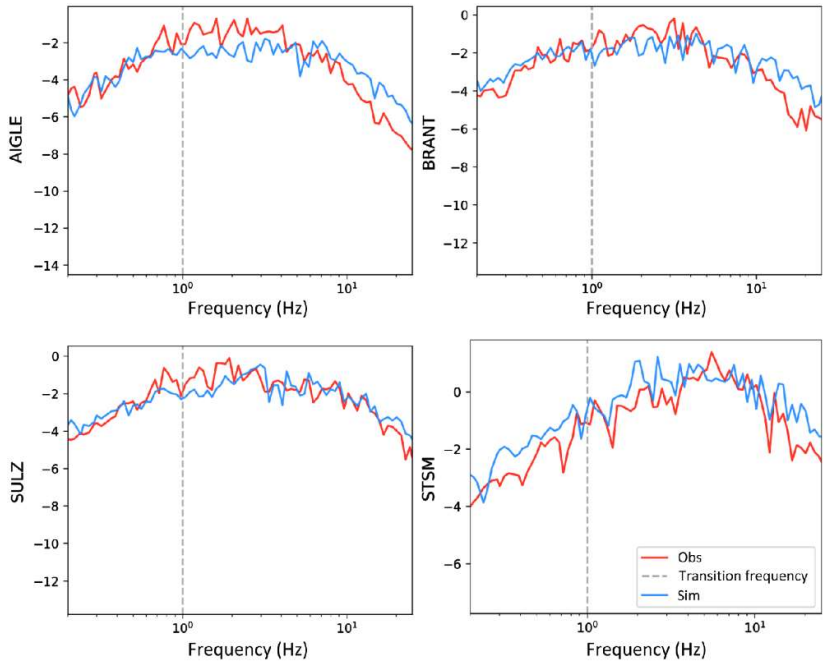

Figure 11. *Comparison of simulated and observed Fourier amplitude spectrum (FAS) at four arbitrary stations for the 2003 M_w 4.8 St Dié event. Note that the y axis is in log10 units.*

represented with our V_{S30}-based site adjustment factors beyond 1000 m/s.

Performance for the three additional events

To deepen our understanding of the performance of the adopted method and the parameters, we present a summary of the simulation results for the 2004 M_w 4.7 Waldkirch, 2004 M_w 4.5 Besançon, and 2005 M_w 4.5 Vallorcine earthquakes at 22, 32, and 15 rock sites, respectively. The source and station distributions are shown in Figure 9. The number of sites is based on the availability and quality of the ground-motion recordings for each event. The source parameters used in the simulations are shown in Table 1, which are taken from Fréchet et al. (2011) for the 2005 Vallorcine event, and Baer et al. (2005) for both the 2004 M_w 4.7 Waldkirch and the 2004 Besançon events. The adopted stress parameters for the HF computation are 12, 7, and 3 MPa, respectively. Figures 13–15 present the simulation results for each of these three earthquakes in terms of time series, FAS, and SA. In general, the overall fit between the simulations and observations is acceptable for all events. For most of the stations, the amplitude and the arrival of the *P*- and *S*-wave packets for simulations and observations are well correlated. We also observe that a few stations have some discrepancies in terms of amplitude. The recordings at station GIMEL for the 2004 Besançon event (Fig. 15), for instance, has an acceleration amplitude about four times larger than the station at a similar distance range (STBU), although, the simulations do not capture this large variation in amplitude. This station is located close to the edge of the Jura Mountain, and this large amplitude could be due to a high-impedance contrast between shallow structures and the underlying rock (Edwards et al., 2013). Similar phenomena have been observed at station HVSC, during the 2010–2011 Canterbury earthquake sequence (Jeong and Bradley, 2017).

It is important to note that we do not expect to capture all the detailed characteristics of the waveforms, given our model's simplicity. The FAS comparisons also show that the simulation matches reasonably well the observations for most of the stations. However, there are few stations (e.g., SULZ for the Vallorcine event) that show some differences in terms of FAS, with higher observations over the intermediate frequency (0.7–2 Hz). Similarly, some

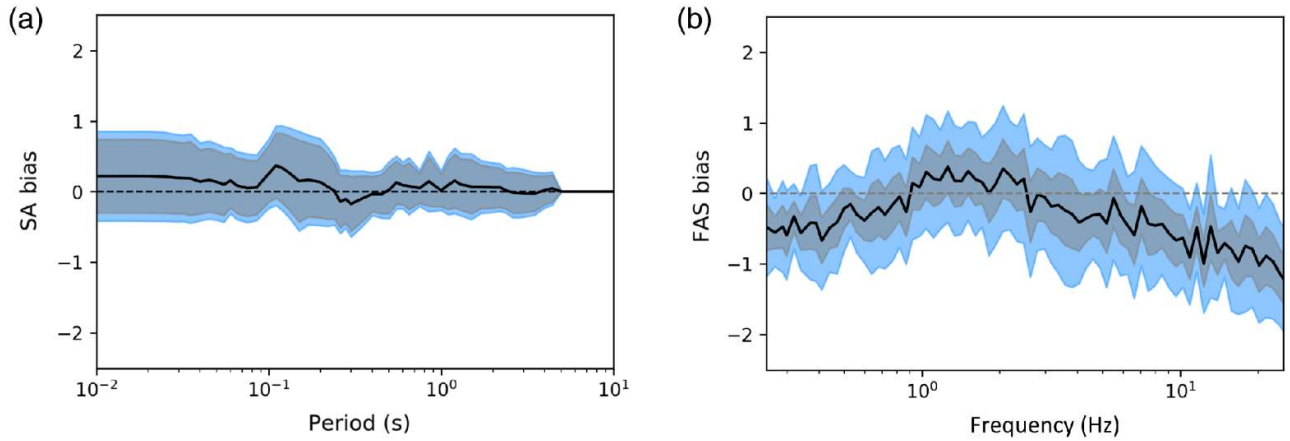

Figure 12. *Goodness of fit of recorded and simulated ground motion for the St Dié earthquake in terms of (a) SA and (b) FAS. The black line shows the model bias in natural log units, the blue and gray zones denote the standard deviation and the 90% confidence interval of the mean, respectively.*

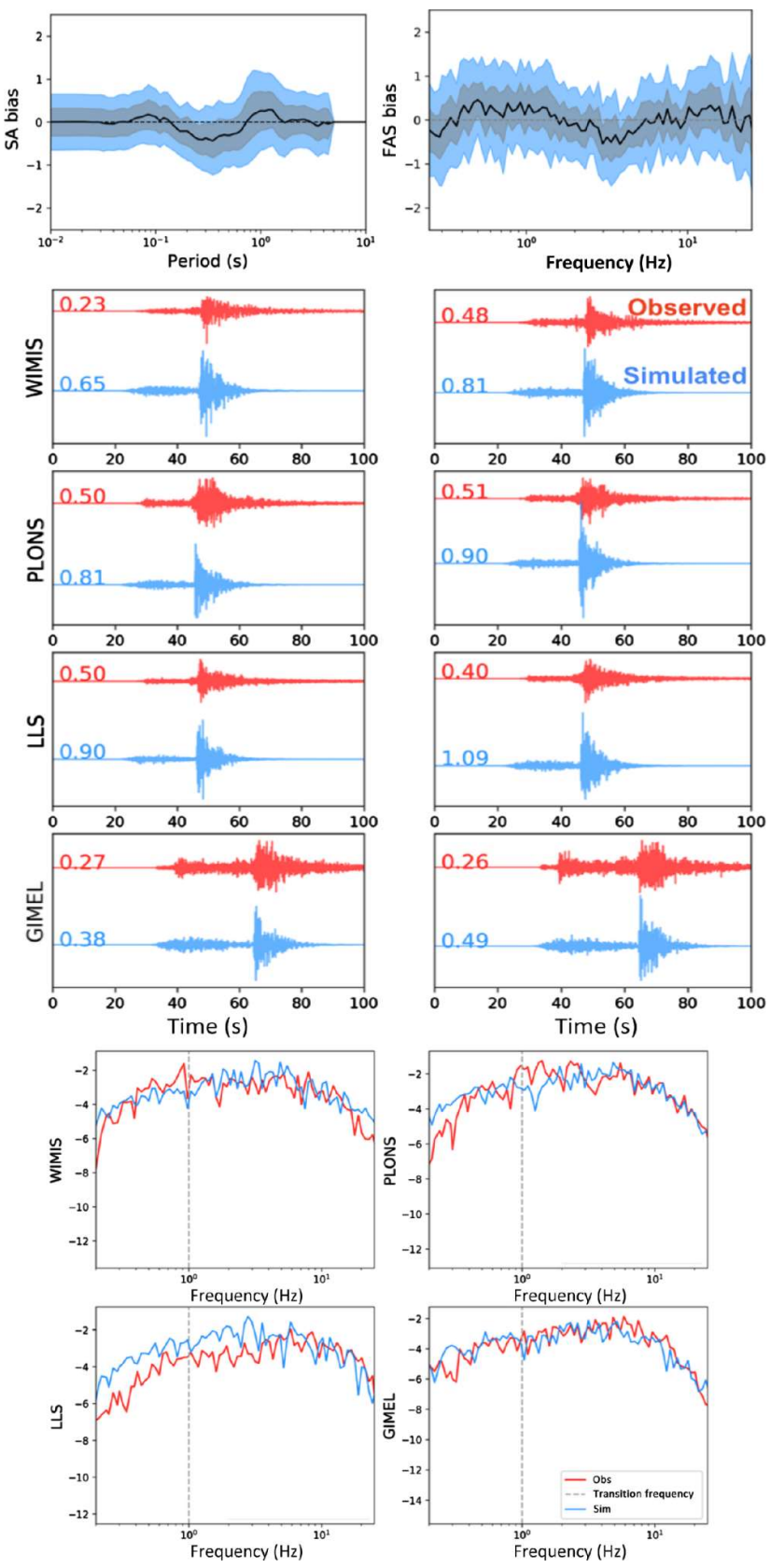

Figure 13. *Summary of the simulation results for the 2004 Waldkirch event: (top) acceleration time series with the corresponding Fourier spectra; (bottom) goodness of fits in terms of SA and FAS. Note that the y axis of FAS is in log10 units. Synthetic seismograms are denoted in blue, and observations are in red. The maximum acceleration (cm/s²) for each waveform is shown above each trace.*

stations (e.g., BRANT, AIGLE) also show differences at higher frequencies (>10 Hz), which is beyond the frequency that the simulations are able to model.

To have a quantitative comparison, we also summarize the bias and variability of the total residuals (mean and standard deviation) in terms of SA and FAS derived from the acceleration waveforms. Noticeable differences appear between the biases from these three events. For the Waldkirch event, Figure 13 shows no significant SA bias for periods $T < 0.2$ s and $T > 1$ s. Beyond this period range, the simulations overestimate the observed amplitudes. For the Vallorcine event, on the other hand, the goodness of fit of the resulting strong-motion simulations shows only small systematic bias in the prediction of the response spectra (Fig. 14). The model predicts well at short periods, up to roughly $T = 0.5$ s. Then, we observe small levels of under- and overprediction at a period of about 0.7–1 s and 2.5 s, respectively. The FAS residuals, on the other hand, show that outside the range of 0.25–10 Hz, our simulations are overpredicting the ground motions, with a standard deviation of about 0.9. Finally, for the Besançon simulation, the SA bias shows that, on average, the simulated values have near-zero mean bias, indicating that the simulated SA is consistent with the ground-motion recordings. The distribution of the SA residuals with respect to distance for all events (Fig. S3) also shows no significant bias for SA at long-vibration periods. For SA at short periods, on the other hand, we observe a small level of distance dependence at large distances (>200 km), which is expected because the reliability of the attenuation model itself is limited at large distances, particularly, at HF (Bindi and Kotha, 2020). The simulations also slightly overpredict the SA [$T < 0.2$ s] values at shorter distances. The standard error ranges from about 0.4–0.8 natural log units, with larger values over the longer periods. The FAS

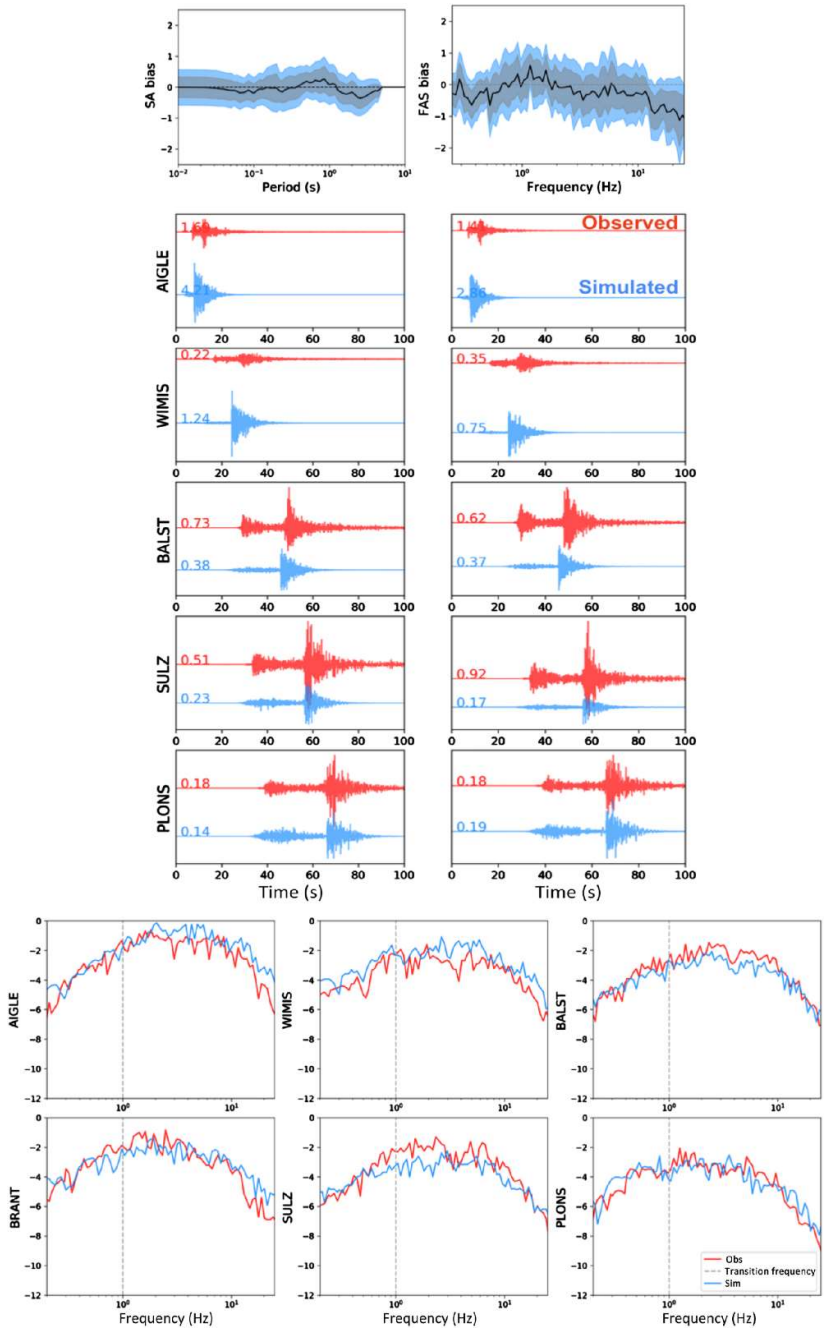

Figure 14. *Summary of the simulation results for the 2005 Vallorcine event: acceleration time series with the corresponding Fourier spectra; goodness of fits in terms of SA and FAS. Note that the y axis of FAS is in log10 units. The maximum acceleration (cm/s²) for each waveform is shown above each trace.*

bias, on the other hand, shows bias fluctuating around zero within the frequency range of 0.3–8 Hz. Beyond this frequency range, the simulations mostly overestimate the observed amplitudes.

Comparison with empirical GMM

Given that empirical GMMs are still commonly used in the hazard assessment and engineering communities, we also assess the performance of the simulation with respect to the empirical GMM, in addition to the comparison between observed and simulated ground motion. The empirical prediction models considered in this study are based on Bindi et al. (2017), which were calibrated for the hazard application in moderate- and low-seismicity areas. Figure 16 compares the consistency between simulations, recordings, and empirical ground motions (in terms of PGA and SA for vibration periods of 0.2, 0.5, and 3 s), as a function of source-to-site distance for the four events and considering rock stations. The median and the standard deviation of the Bindi et al. (2017) empirical GMM (V_{S3} = 800 m/s) are displayed as thick and thin lines, respectively. In general, the simulated ground motion follows the trend of the data and the empirical GMM. However, the simulations appear to predict better the attenuation of the observed ground motions. For the 2004 M_w 4.7 Waldkirch event, for instance, we observe that between 60 and 120 km, both the simulations and the observations exceed the predictions from the empirical GMM, and their amplitudes do not attenuate significantly. Then, beyond 120 km, they follow the trend of the empirical GMM again. Such flattened attenuation between 60 and 120 km, which is well captured by the simulations, was also reported by previous studies for various regions and has been interpreted to be due to the amplifying effects from the arrivals of critically reflected S-waves off the Mohorovicic discontinuity, that is, critical reflection from the lower crust (e.g., California, Somerville and Yoshimura, 1990; northwestern Turkey, Bindi et al., 2007). Such phenomena are not expected for every earthquake, as they are controlled by many factors, including magnitude, focal depth, and source mechanism. For the 2003 St Dié event, for instance, such a phenomenon is not as striking as for the 2004 M_w 4.7 Waldkirch event. Regarding the spread of the ground-motion predictions in Figure 16, all three predictions show noticeable differences for various intensity measures. The variability is comparably less for PGA than for SA at longer periods (e.g., SA[T = 3 s]), which illustrates the period dependency of ground-motion variability. It has been noted that this feature

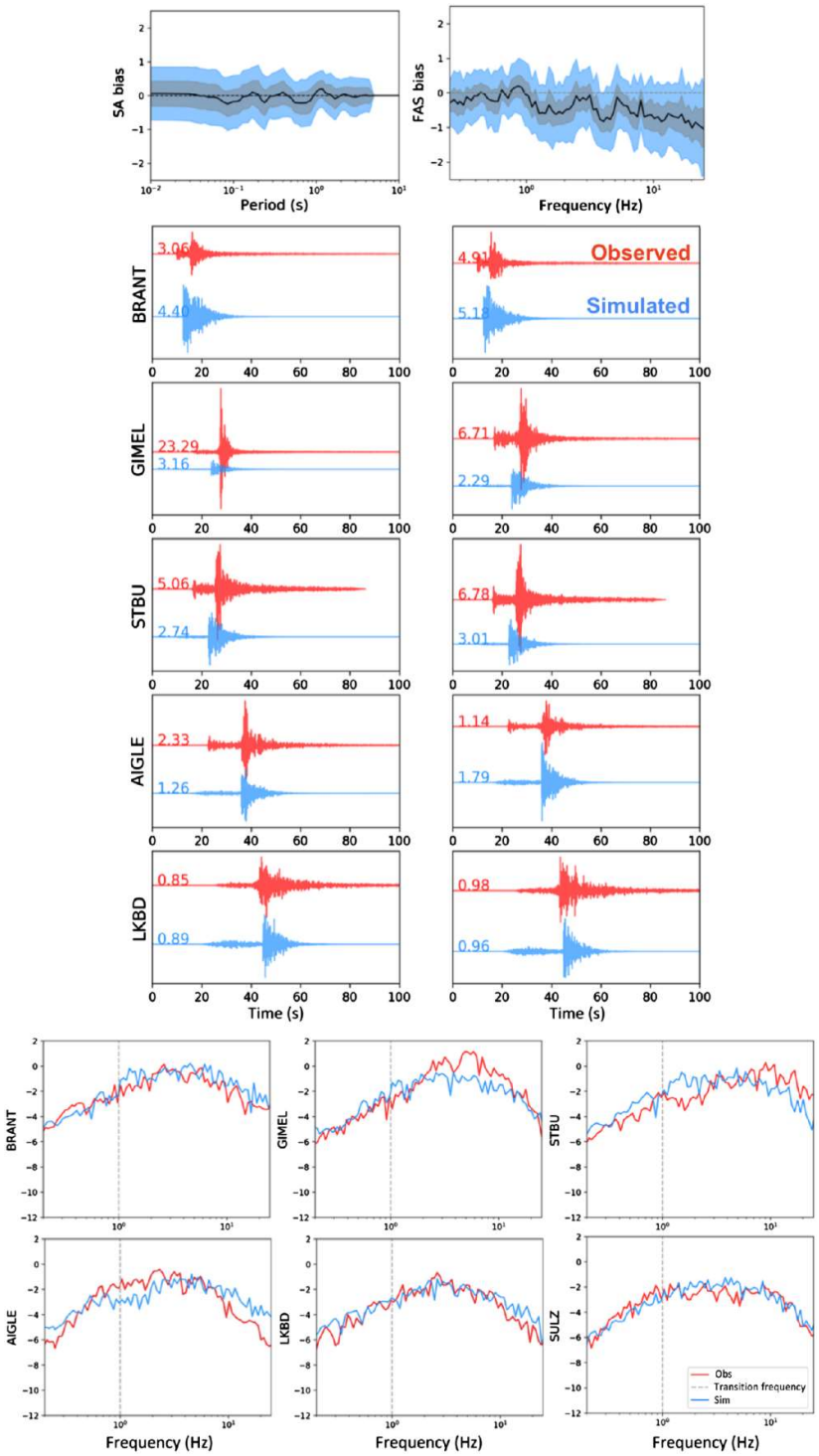

Figure 15. *Summary of the simulation results for simulation results of the 2004 Besançon event: acceleration time series with the corresponding Fourier spectra; goodness of fits in terms of SA and FAS. The maximum acceleration (cm/s²) for each waveform is shown above each trace.*

might also be due to distance-dependent apparent geometrical decay functions (e.g., Atkinson and Mereu, 1992).

VALIDATION AT ALL SITES IN TERMS OF FAS

To assess the salient aspects for the ground motion under various near-surface site amplification conditions, simulations are performed at reference sites (rock) for all sites. Subsequently, three different empirical site amplifications are applied. To emphasize the relative effect of these factors on ground motion, and without any potential contamination due to the introduction of random phase, we focus on the validation in terms of FAS (physical measure). Figure 17 plots the FAS of the observations along with the simulated ground motion applying the three amplification factors at station OGEP V_{S30} = (350 m/s) for the 2003 St Dié event, as well as at station BOURR (V_{S30} = 694 m=s) for the 2003 St Dié and 2004 Waldkirch events. We, particularly, choose BOURR, because it is a station where the V_{S3} was reported to capture the site effects easily, which is not always the case. Figure 17 shows that the use of site-specific amplification factors improves the FAS fits, especially at intermediate frequencies (f = 1–4 Hz). This result is consistent with Fäh, Fritsche, et al. (2009), who investigated the site information for SED stations and observed that the H/V peak for station BOURR is at around f = 2 Hz. We also observed that only minor differences appear between the ground motions derived by applying the two V_{S30}-based (SA and Fourier) site amplifications. Such differences occur mainly at frequencies less than about 3 Hz. At frequencies above 3 Hz, SA and Fourier models are nearly identical. To further quantify the goodness of fit of the simulations with the observations for all sites, Figure 18 presents the FAS bias for the St Dié and Waldkirch events computed from 35 and 40 stations, respectively, for V_{S3} -based site amplification cases. These stations are located in various site conditions, with V_{S30} ranging from 342 to 2925 m/s. For the site-specific case, the FAS bias is computed using 12 stations. This is because the site-specific ones are not available for all stations, as mentioned in the site amplification description. Despite these differences, we find that the pattern of the FAS bias for the three cases follows the general pattern for the rock site, with only minor

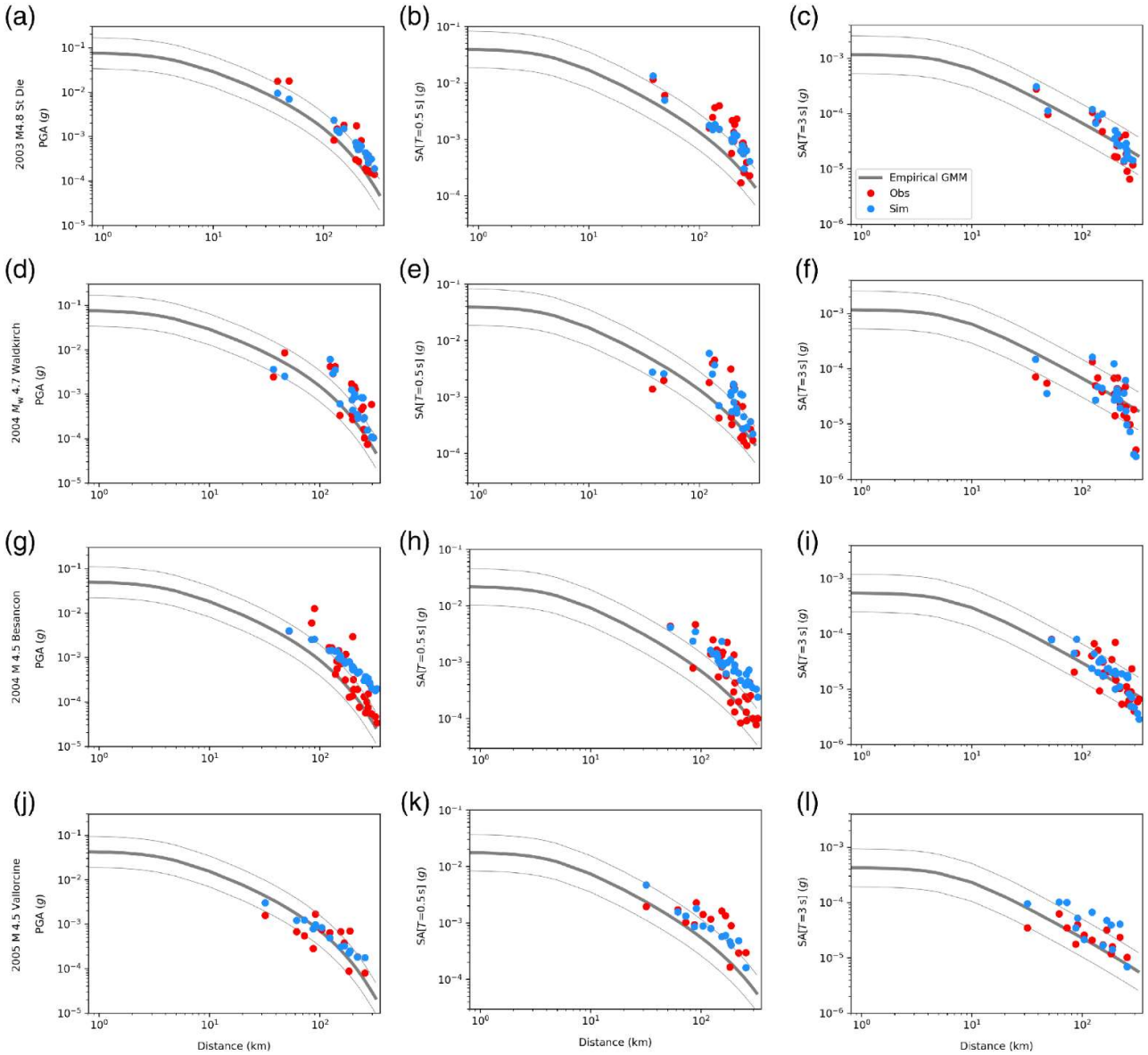

Figure 16. *Comparison of the recorded, simulated, and empirical ground motion (peak ground acceleration [PGA], SA [0.5 s], SA [3 s]) as a function of source-to-site distance for the (a–c) 2003 St Dié, (d–f) 2004 Waldkirch, (g–i) 2004 Besancon, and (j–l) 2005 Vallorcine events.*

differences for the V_{S30}-based site amplifications. The site-specific ones, on the other hand, are shifted toward lower values, yielding a bias closer to zero, particularly, over intermediate frequencies $f = 0.7$–2 Hz.

DISCUSSION AND CONCLUSION

Motivated by the lack of strong ground motion recordings, particularly, in moderate seismicity regions and the need for robust ground-motion predictions for engineering applications, we conducted ground-motion simulations in the URG using moderate magnitude events. The simulations were performed using the GP method tailored for the stable continental region in Europe. The fundamental modifications involved: (1) the calibration of anelastic attenuation through fitting European spectral decomposition results; (2) the incorporation of P waves into the HF computation; and (3) the implementation of Fourier-based V_{S3} and site-specific near-surface site amplification. The simulation results were assessed using the ground-motion recordings from four events in the URG area: the 2003 M_w 4.8 St. Dié, the 2004 M_w 4.7 Waldkirch, the 2004 M_w 4.5 Besançon, and the 2005 M_w 4.5 Vallorcine earthquakes. Previously, the GP method has been extensively validated for large events in high-seismicity regions. In this study, we calibrate, test, and validate the applicability of the GP method for the most significant recorded earthquakes in the URG area. These earthquakes are, however, of moderate size, which means that these tests and calibrations are performed for relatively small finite-fault ruptures. Such calibration helps to better predict the ground

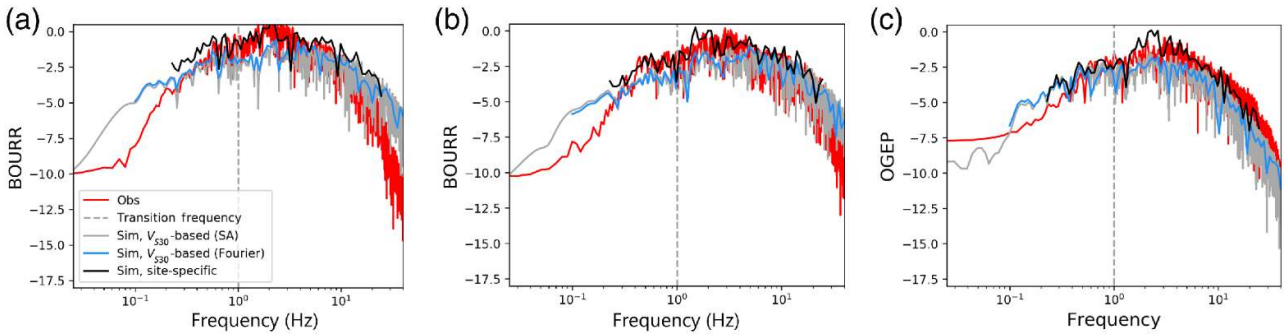

Figure 17. *Comparison of FAS for observed and simulated ground motion from (a) the 2003 St Dié event, as observed at BOURR, (b) the 2004 Waldkirch earthquake at BOURR, and (c) the 2003 St Dié event at OGEP station.*

shaking of future moderate earthquakes and also calibrates the HF attenuation part, which will be critical for large earthquakes, too. It is indeed foreseen that the developed method and its regional adjustments will be used to simulate large earthquakes, with magnitude beyond the magnitude used in this simplicity of the adopted velocity structure.

Regarding the calibration of the anelastic attenuation, it appears to affect the SA bias over all periods (as shown in Fig. 5). Similar behavior is observed when varying the stress parameter, which is another important term in the HF computation. Figure 19

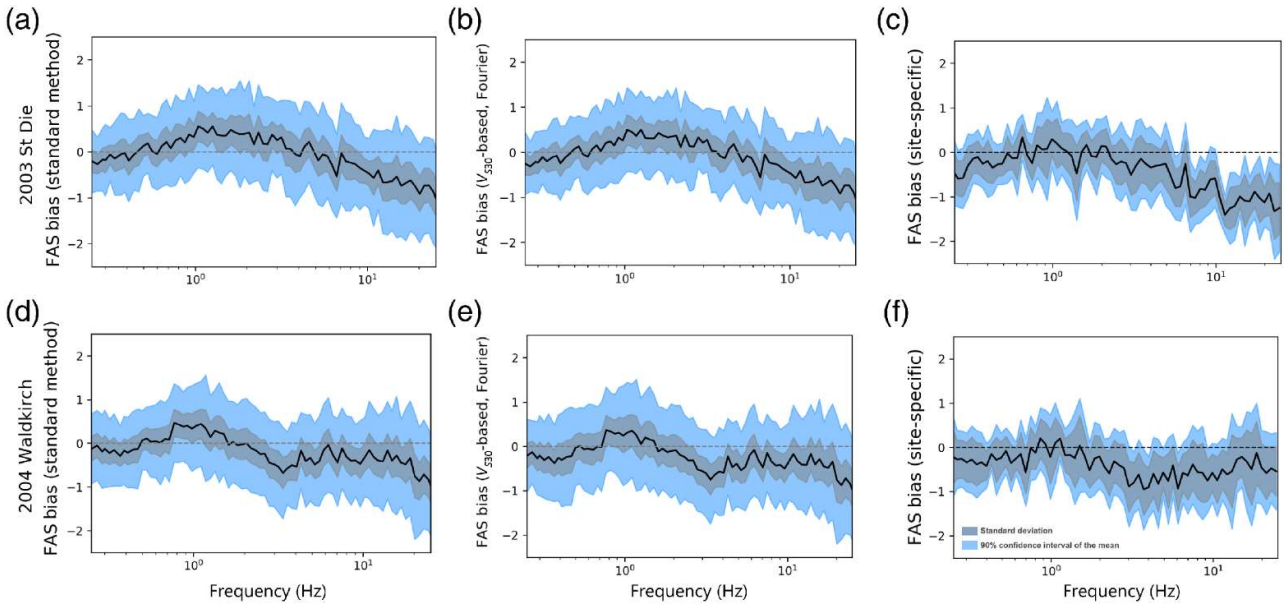

Figure 18. *Comparison of the FAS bias from the three different site amplification factors: Standard method (SA-based V_{S30}), Fourier-based V_{S30}, and site-specific for (a–c) the 2003 St Dié and (d–f) the 2004 Waldkirch earthquakes. The thick line depicts the median.*

testing exercise.

We found that, in general, the modification in the HF part (e.g., incorporation of *P* waves) was necessary to improve the fit with observations of these events in the time domain. Although, the simulations captured the main features of the observations (see the waveform comparisons in Figs. 10, 13–15), some differences appear in terms of the arrival times at some stations. Table 3 statistically summarizes the arrival-time residuals from the simulations and observations for all four events. Discrepancies were both positive and negative, but generally considered to be acceptable. They are due to various factors, including earthquake location uncertainties and the shows the SA bias for the 2003 St Dié event by varying the stress parameter from 7 to 13 MPa. The stress parameter used in all previous simulations for this event is 10 MPa. Therefore, rigorous uncertainty analyses are still needed to evaluate the trade-offs between these two components, which are left for

TABLE 3
Mean and Standard Deviation of the Arrival-Time Residuals for the Studied Events

Event	Mean	Standard Deviation
St Dié	0.77	1.43
Waldkirch	-1.89	3.68
Vallorcine	0.44	2.03
Besançon	1.29	1.78

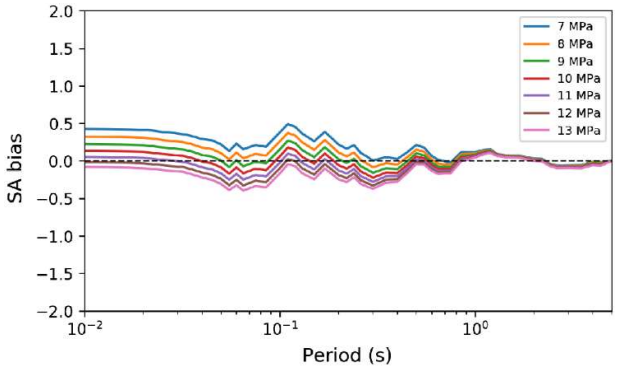

Figure 19. *Effects of variations in the stress parameter on the SA residuals for the 2003 M_w 4.8 St Dié event.*

future investigations.

In this study, we have focused on event-specific stress parameters, which were among the data produced by Bindi and Kotha (2020), to derive the magnitude dependent model in Figure 3. Hence, our findings validate the fact that parameters from the spectral decomposition are giving well-calibrated time histories (in terms of frequency and amplitude) when used as input parameters of the broadband simulations. For simulation of future earthquakes, instead of using event-specific stress drops, we could use the average stress drops taken from the distribution of the stress drops derived by Bindi and Kotha (2020). Furthermore, robust and well-calibrated relations among stress drops, magnitude, and depth are currently under development, using analysis of large datasets (e.g., Zaccarelli et al., 2019). Such scaling relationships of the stress drop with other source parameters would be an additional feature for merging the deterministic LF and semistochastic HF in the hybrid method.

The ground-motion validation on rock sites, adopted as a first step in the validation, is crucial to facilitate the implementation and testing of various near-surface site amplification models. For instance, it avoids the necessity of deconvolution that could produce potential errors, especially when there is a lack of information about the amplification parameters previously used. As ground motions on rock sites are often used as the reference motion in seismic hazard analyses, such validation should be an essential element of any ground-motion validation process.

This study has tested three site-amplification factors: the V_{S30}-based (SA) in the standard GP method, Fourier V_{S30}-based, and site-specific amplification factors. The site-specific method improves the fits to the observations, particularly, in the frequency range 0.5–2 Hz in which local site effects are significant for most of the stations. Despite those benefits, it is essential that these amplification models are either empirical or only available at sites with existing seismic stations. Therefore, future potential improvements following this study would be to explicitly model site amplification (e.g., Roten et al., 2012) and adjust the time-series models accordingly. For instance, Pilz, Cotton, et al. (2021) showed the benefits of such an approach, especially in a region with a thick sedimentary basin, such as the Cologne area (Germany). de la Torre et al. (2020) also showed that the use of 1D site response models in the simulation of the Canterbury earthquakes reduces the systematic residuals at sites that exhibit strong site amplification.

The findings in this study support the incorporation of scenario-based ground-motion simulations for use in the characterization of seismic hazard and other engineering applications. Following the validation, we could confidently use the approach to generate time histories for hazard and risk analyses, and to complement the data in the surrounding area that lack seismic stations and recordings. The combination of recordings and simulation-based ground motions would allow the development of a new generation of GMMs that could better constrain predictions in the near-source area and those regions with sparse ground-motion data.

DATA AND RESOURCES

The recorded ground motion and site information are from European Integrated Data Archive (EIDA, https://www.orfeus-eu.org/data/eida, last accessed January 2021), and the engineering strong-motion flat file (ESM, https://esm.mi.ingv.it//flatfile-2018/, last accessed January 2021). In particular, we used waveforms recorded by networks GR (Federal Institute for Geosciences and Natural Resources [BGR], 1976), RA (RESIF, 1995), CH (Swiss Seismological Service [SED] At ETH Zurich, 1983). The recorded ground motions were retrieved through stream2-segment, which is an open-source tool for downloading, visualizing, and processing seismic waveforms (see details in Zaccarelli et al., 2019). Simulations were performed through the Southern California Earthquake Center (SCEC) broadband platform available at https://github.com/SCECcode/bbp (last accessed August 2020). The supplementary material contains figures of the crustal velocity model used to generate the Green's function, simulation results at station BRANT to highlights the need of compressional wave, and the overall SA residuals at three different vibration periods for the simulation of the 2003 M_w 4.8 St Dié, the 2004 M_w 4.7Waldkirch, the 2004 M_w 4.5 Besançon, and the 2005 M_w 4.5 Vallorcine earthquakes.

DECLARATION OF COMPETING INTERESTS

The authors acknowledge that there are no conflicts of interest recorded.

ACKNOWLEDGMENTS

The authors would like to thank Fabio Silva of the Southern California Earthquake Center (SCEC) for his assistance in setting up the new velocity model in the

broadband platform (BBP). The authors also thank Art Frankel, Morgan Moschetti, Kim Olsen, one anonymous reviewer, and Associate Editor Luis Angel Dalguer for their constructive suggestions and comments that helped to improve the article. This work has been partly funded by the Euratom research and training programme, under the project METIS grant no. 945121.

REFERENCES

Anderson, J. G. (2015). The composite source model for broadband simulations of strong ground motions, Seismol. Res. Lett. 86, 68–74.

Anderson, J. G., and S. E. Hough (1984). A model for the shape of the Fourier amplitude spectrum of acceleration at high frequencies, Bull. Seismol. Soc. Am. 74, 1969–1993.

Arias, A. (1970). A measure of earthquake intensity, in Seismic Design for Nuclear Power Plants, R. J. Hansen (Editor), MIT Press, Cambridge, Massachusetts, 438–483.

Atkinson, G., and K. Assatourians (2015). Implementation and validation of EXSIM (A stochastic finite-fault ground-motion simulation algorithm) on the SCEC broadband platform, Seismol. Res. Lett. 86, 48–60.

Atkinson, G., and R. Mereu (1992). The shape of ground motion attenuation curves in Southeastern Canada, Bull. Seismol. Soc. Am. 82, 2014–2031.

Baer, M., N. Deichmann, J. Braunmiller, S. Husen, D. Fäh, D. Giardini, P. Kästli, U. Kradolfer, and S. Wiemer (2005). Earthquakes in Switzerland and surrounding regions during 2004, Eclogae Geol. Helv. 98, 407–418.

Bindi, D., and S. R. Kotha (2020). Spectral decomposition of the engineering strong motion (ESM) flat file: Regional attenuation, source scaling and arias stress drop, Bull. Earthq. Eng. 18, 2581–2606.

Bindi, D., F. Cotton, S. R. Kotha, C. Bosse, D. Stromeyer, and G. Grünthal (2017). Application-driven ground motion prediction equation for seismic hazard assessments in non-cratonic moderate-seismicity areas, J. Seismol. 21, 1201–1218.

Bindi, D., S. Parolai, H. Grosser, C. Milkereit, and E. Durukal (2007). Empirical ground-motion prediction equations for northwestern Turkey using the aftershocks of the 1999 Kocaeli earthquake, Geophys. Res. Lett. 34, no. L08, 305.

Bindi, D., G. Weatherill, G. Lanzano, L. Luzi, and F. Cotton (2019). The pan-European engineering strong motion (ESM) flatfile: Consistency check via residual analysis, Bull. Earthq. Eng. 17, 583–602.

Boore, D. M. (1983). Stochastic simulation of high-frequency ground motions based on seismological models of the radiated spectra, Bull. Seismol. Soc. Am. 73, 1865–1894.

Bora, S. S., F. Cotton, and F. Scherbaum (2019). NGA-West2 empirical Fourier and duration models to generate adjustable response spectra, Earthq. Spectra 35, 61–93.

Bora, S., F. Cotton, F. Scherbaum, B. Edwards, and P. Traversa (2017). Stochastic source, path and site attenuation parameters and associated variabilities for shallow crustal European earthquakes, Bull. Earthq. Eng. 15, 4531–4561.

Bydlon, S. A., K. B. Withers, and E. M. Dunham (2019). Combining dynamic rupture simulations with ground-motion data to characterize seismic hazard from 3 to 5.8 earthquakes in Oklahoma and Kansas, Bull. Seismol. Soc. Am. 109, 652–671.

Campbell, K. W., and Y. Bozorgnia (2014). NGA-West2 ground motion model for the average horizontal components of PGA, PGV, and 5% damped linear acceleration response spectra, Earthq. Spectra 30, 1087–1115.

Cara, M., A. Schlupp, and C. Sira (2007). Observations sismologiques: Sismicité de la France en 2003, 2004, 2005, Bureau central sismologique français, ULP/EOST – CNRS/INSU, Strasbourg, France (in French).

Chen, D.-Y., T.-L. Lin, Y.-M. Wu, and N.-C. Hsiao (2012). Testing a P-wave earthquake early warning system by simulating the 1999 Chi-Chi, Taiwan, Mw 7.6 earthquake, Seismol. Res. Lett. 83, 103–108.

Crempien, J. G. F., and R. J. Archuleta (2015). UCSB method for simulation of broadband ground motion from kinematic earthquake sources, Seismol. Res. Lett. 86, 61–67.

Deichmann, N., M. Baer, J. Braunmiller, S. Husen, D. Faeh, D. Giardini, P. Kaestli, U. Kradolfer, and S. Wiemer (2006). Earthquakes in Switzerland and surrounding regions during 2005, Eclogae Geol. Helv. 99, 443–452.

de la Torre, C., B. Bradley, and R. Lee (2020). Modeling nonlinear site effects in physics-based ground motion simulations of the 2010-2011 Canterbury earthquake sequence, Earthq. Spectra 36, 856–879.

Dominique, P., and B. Le Brun (2003). Le séisme de Rambewillers (Vosges) du 22 février 2003, Mission post sismique., BRGM/RP-52273-FR, 39 pp (in French).

Dreger, D. S., and T. H. Jordan (2015). Introduction to the focus section on validation of the SCEC Broadband Platform V14.3 simulation methods, Seismol. Res. Lett. 86, 15–16.

Edwards, B., D. Fäh, and D. Giardini (2011). Attenuation of seismic shear wave energy in Switzerland, Geophys. J. Int. 185, 967–984.

Edwards, B., C. Michel, V. Poggi, and D. Fäh (2013). Determination of site amplification from regional seismicity: Application to the Swiss national seismic networks, Seismol. Res. Lett. 84, 611–621.

Fäh, D., S. Fritsche, V. Poggi, G. Gassner-Stamm, P. Kästli, J. Burjanek, P. Zweifel, S. Barman, and J. Clinton (2009). Determination of site information for seismic stations in Switzerland, Work package 4: Pegasos Refinement Project, Swiss Seismological Service ETH Zürich, Report SED/PRP/R/004/20090831.

Fäh, D., M. Gisler, B. Jaggi, P. Kästli, T. Lutz, V. Masciadri, C. Matt, D. Mayer-Rosa, D. Rippmann, G. Schwarz-Zanetti, et al. (2009). The 1356 Basel earthquake: An interdisciplinary revision, Geophys. J. Int. 178, 351–374.

Federal Institute for Geosciences and Natural Resources (1976). German Regional Seismic Network (GRSN), Bundesanstalt für Geowissenschaften und Rohstoffe, doi: 10.25928/mbx6-hr7.

Frankel, A. (2009). A constant stress-drop model for producing broadband synthetic seismograms: Comparison with the Next Generation Attenuation relations, Bull. Seismol. Soc. Am. 99, 664–680.

Fréchet, J., F. Thouvenot, M. Frogneux, N. Deichmann, and M. Cara (2011). The Mw 4.5 Vallorcine (French Alps) earthquake of 8 September 2005 and its complex aftershock sequence, J. Seismol. 15, 43–58.

Goulet, C. A., N. A. Abrahamson, P. G. Somerville, and K. E. Woodell (2015). The SCEC broadband platform validation exercise for pseudospectral acceleration: Methodology for code validation in the context of seismic hazard analyses, Seismol. Res. Lett. 86, 17–26.

Graves, R. W., and A. Pitarka (2010). Broadband ground motion simulation using a hybrid approach, Bull. Seismol. Soc. Am. 100, 2095–2123.

Graves, R. W., and A. Pitarka (2015). Refinements to the Graves and Pitarka (2010) broadband ground-motion simulation method, Seismol. Res. Lett. 86, 75–80.

Graves, R. W., and A. Pitarka (2016). Kinematic ground-motion simulations on rough faults including effects of 3D stochastic velocity perturbations, Bull. Seismol. Soc. Am. 106, 2136–2153.

Grünthal, G., and R. Wahlström (2012). The European-Mediterranean earthquake catalogue (EMEC) for the last millennium, J. Seismol. 16, 535–570.

Grünthal, G., R. M. W. Musson, J. Schwarz, and M. Stucchi (1998). European Macroseismic Scale 1998 (EMS-98), Serie: Cahiers du Centre européen de géodynamique et de séismologie, Vol. 15, European Centre for Geodynamics and Seismology, Luxembourg, p. 99.

Grünthal, G., D. Stromeyer, C. Bosse, F. Cotton, and D. Bindi (2018). The probabilistic seismic hazard assessment of Germany-Version 2016, considering the range of epistemic uncertainties and aleatory variability, Bull. Earthq. Eng. 16, 4339–4395.

Hartzell, S. (1978). Earthquake aftershocks as Green's functions, Geophys. Res. Lett. 5, 1–4.

Havenith, H.-B., D. Fäh, U. Polom, and A. Roullé (2007). S-wave velocity measurements applied to the seismic microzonation of Basel, Upper Rhine Graben, Geophys. J. Int. 170, 346–358.

Hintersberger, E., F. Scherbaum, and S. Hainzl (2007). Update of likelihood-based ground-motion model selection for seismic hazard analysis in western central Europe, Bull. Earthq. Eng. 5, 1–16.

Jeong, S., and B. Bradley (2017). Amplification of strong ground motions at Heathcote Valley during the 2010–2011 Canterbury Earthquakes: The role of 2d nonlinear site response, Bull. Seismol. Soc. Am. 107, 2117–2130.

Kramer, S., and R. Mitchell (2006). Ground motion intensity measures for liquefaction hazard evaluation, Earthq. Spectra 22, 413–438.

Lee, R., B. Bradley, P. Stafford, R. Graves, and A. Rodriguez-Marek (2020). Hybrid broadband ground motion simulation validation of small magnitude earthquakes in Canterbury, New Zealand, Earthq. Spectra 36, 1–27.

Leonard, M. (2014). Self-consistent earthquake fault-scaling relations: Update and extension to stable continental strike-slip faults, Bull. Seismol. Soc. Am. 104, 2953–2965.

Liu, P., R. J. Archuleta, and S. H. Hartzell (2006). Prediction of broadband ground-motion time histories: Hybrid low/high-frequency method with correlated random source parameters, Bull. Seismol. Soc. Am. 96, 2118–2130.

Lombardi, D., J. Braunmiller, E. Kissling, and D. Giardini (2008). Moho depth and Poisson's ratio in the Western–Central Alps from receiver functions, Geophys. J. Int. 173, 249–264.

Mai, P. M., W. Imperatori, and K. B. Olsen (2010). Hybrid broadband ground-motion simulations: Combining long-period deterministic synthetics with high-frequency multiple S-to-S backscattering, Bull. Seismol. Soc. Am. 101, 2124–2142.

Molliex, S., O. Fabbri, V. Bichet, and H. Madritsch (2011). Possible quaternary growth of a hidden anticline at the front of the Jura fold-and-thrust belt: Geomorphological constraints from the Foret de Chaux area, France, Bull. Soc. Géol. Fr. 182, 337–346.

Nivière, B., A. Bruestle, G. Bertrand, S. Carretier, J. Behrmann, and J.-C. Gourry (2008). Active tectonics of the southeastern Upper Rhine Graben, Freiburg area (Germany), Quaternary Sci. Rev. 27, 541–555.

Olsen, K., and R. Takedatsu (2014). The SDSU broadband ground motion generation module BBtoolbox version 1.5, Seismol. Res. Lett. 86, 81–88.

Olsen, K. B., and J. E. Mayhew (2010). Goodness-of-fit criteria for broadband synthetic seismograms, with application to the 2008 Mw 5.4 Chino Hills, California, earthquake, Seismol. Res. Lett. 81, 715–723.

Oth, A., S. Parolai, and D. Bindi (2011). Spectral analysis of K-NET and KiK-net Data in Japan, Part I: Database compilation and peculiarities, Bull. Seismol. Soc. Am. 101, 652–666.

Pilz, M., F. Cotton, and S. R. Kotha (2020). Data-driven and machine learning identification of seismic reference stations in Europe, Geophys. J. Int. 222, 861–873.

Pilz, M., F. Cotton, H. N. T. Razafindrakoto, G. Weatherill, and T. Spies (2021). Regional broadband ground-shaking modelling over extended and thick sedimentary basins: An example from the Lower Rhine Embayment (Germany), Bull. Earthq. Eng. 19, 581–603.

Pousse, G., L. F. Bonilla, F. Cotton, and L. Margerin (2006). Nonstationary stochastic simulation of strong ground motion time histories including natural variability: Application to the K-Net Japanese database, Bull. Seismol. Soc. Am. 96, 2103–2117.

Razafindrakoto, H., B. Bradley, and R. Graves (2018). Broadband ground-motion simulation of the 2011 Mw 6.2 Christchurch, New Zealand, earthquake, Bull. Seismol. Soc. Am. 108, 2130–2147.

RESIF (1995). RESIF-RAP French accelerometric network, RESIFRAP strong motion network and other seismic stations in metropolitan France [Data set]. RESIF - Réseau Sismologique et géodésique Français, doi: 10.15778/RESIF.FR.

Roten, D., K. Olsen, and J. Pechmann (2012). 3D simulations of M7 earthquakes on the Wasatch Fault, Utah, Part II: Broadband (0-10 Hz) ground motions and nonlinear soil behavior, Bull. Seismol. Soc. Am. 102, 2008–2030.

Rotstein, Y., and M. Schaming (2011). The Upper Rhine Graben (URG) revisited: Miocene transtension and transpression account for the observed first-order structures, Tectonophysics 30, TC3007, doi: 10.1029/2010TC002767.

Rotstein, Y., J. Edel, G. Gabriel, D. Boulanger, M. Schaming, and M. Munschy (2006). Insight into the structure of the Upper Rhine Graben and its basement from a new compilation of Bouguer gravity, Tectonophysics 425, 55–70.

Sandikkaya, M. A., and S. Akkar (2017). Cumulative absolute velocity, Arias intensity and significant duration predictive models from a pan-European strong-motion dataset, Bull. Earthq. Eng. 15, 1–18.

Saragoni, G., and G. Hart (1974). Simulation of artificial earthquakes, Earthq. Eng. Struct. Dynam. 2, 249–267.

Saunders, J. K., and B. Aagaard (2019). Assessing ShakeAlert earthquake early warning performance using California earthquake simulations: Validation metrics from near-field observations, AGU Fall Meeting, Abstract S31C–0514.

Scherbaum, F., F. Cotton, and P. Smit (2004). On the use of response spectral-reference data for the selection and ranking of ground-motion models for seismic-hazard analysis in regions of moderate seismicity: The case of rock motion, Bull. Seismol. Soc. Am. 94, 2164–2185.

Schwarz, J., L. Abrahamczyk, S. Amstein, C. Kaufmann, and T. Langhammer (2006). Das Waldkirch-Erdbeben (Baden-Württemberg) vom 5 Dezember 2004, Bautechnik 83, 202–208 (in German).

Skarlatoudis, A., P. G. Somerville, H. K. Thio, and J. R. Bayless (2015). Broadband strong ground motion simulations of large subduction earthquakes, Bull. Seismol. Soc. Am. 105, 3050–3067.

Somerville, P. G., and J. Yoshimura (1990). The influence of critical Moho reflections on strong ground motions recorded in San Francisco and Oakland during the 1989 Loma Prieta earthquake, Geophys. Res. Lett. 17, 1203–1206.

Swiss Seismological Service (SED) At ETH Zurich (1983). National Seismic Networks of Switzerland, ETH Zürich, doi: 10.12686/sed/networks/ch.

Traversa, P., E. Maufroy, F. Hollender, V. Perron, V. Bremaud, H. Shible, S. Drouet, P. Guéguen, M. Langlais, D. Wolyniec, et al. (2020). RESIF RAP and RLBP dataset of earthquake ground motion in Mainland France, Seismol. Res. Lett. 91, 2409–2424.

Withers, K., K. Olsen, S. Day, and S. Zheqiang (2019). Ground motion and intraevent variability from 3D deterministic broadband (0–7.5 Hz) simulations along a nonplanar strike-slip fault, Bull. Seismol. Soc. Am. 109, 229–250.

Withers, K., K. Olsen, S. Zheqiang, and S. Day (2019). Validation of deterministic broadband ground motion and variability from dynamic rupture simulations of buried thrust earthquakes, Bull. Seismol. Soc. Am. 109, 212–228.

Zaccarelli, R., D. Bindi, A. Strollo, J. Quinteros, and F. Cotton (2019). Stream2segment: An open-source tool for downloading, processing, and visualizing massive event-based seismic waveform datasets, Seismol. Res. Lett. 90, 2028–2038.

Zheqiang, S., and S. Day (2013). Rupture dynamics and ground motion from 3D rough-fault simulations, J. Geophys. Res. 118, 1122–1141.